Impact of Multiple Scattering on Longwave Radiative Transfer Involving Clouds

Chia-Pang Kuo[1], Ping Yang[1], Xianglei Huang[2], Daniel Feldman[3], Mark Flanner[2], Chaincy Kuo[3] and Eli J. Mlawer[4]

[1]Department of Atmospheric Sciences, Texas A&M University, College Station, TX, United States

[2]Department of Atmospheric, Oceanic, and Space Sciences, University of Michigan, Ann Arbor, MI, United States

[3]Lawrence Berkeley National Laboratory, Berkeley, CA, United States

[4]Atmospheric and Environmental Research, Inc., Cambridge, MA, United States

Key Points:

- Global impacts of LW scattering are evaluated by using high spatial resolution satellite-derived cloud properties and top and base heights
- Omitting cloud LW scattering increases annual mean TOA upward flux by 2.6 W/m^2 and decreases annual mean surface downward flux by 1.2 W/m^2
- Including LW scattering of clouds in simulations cools the tropopause approximately 0.018 K/day and heats the surface about 0.028 K/day

For publication in the

Journal of Advances in Modeling Earth Systems

This is the author manuscript accepted for publication and has undergone full peer review but has not been through the copyediting, typesetting, pagination and proofreading process, which may lead to differences between this version and the Version of record. Please cite this article as doi:10.1002/2017MS001117.

Abstract

General circulation models (GCMs) are extensively used to estimate the influence of clouds on the global energy budget and other aspects of climate. Because radiative transfer computations involved in GCMs are costly, it is typical to consider only absorption but not scattering by clouds in longwave (LW) spectral bands. In this study, the flux and heating rate biases due to neglecting the scattering of LW radiation by clouds are quantified by using advanced cloud optical property models, and satellite data from Cloud-Aerosol Lidar and Infrared Pathfinder Satellite Observation (CALIPSO), CloudSat, Clouds and the Earth's Radiant Energy System (CERES) and Moderate Resolution Imaging Spectrometer (MODIS) merged products (CCCM). From the products, information about the atmosphere and clouds (microphysical and buck optical properties, and top and base heights) is used to simulate fluxes and heating rates. One-year global simulations for 2010 show that the LW scattering decreases top-of-atmosphere (TOA) upward flux and increases surface downward flux by 2.6 and 1.2 W/m^2, respectively, or approximately 10% and 5% of the TOA and surface LW cloud radiative effect, respectively. Regional TOA upward flux biases are as much as 5% of global averaged outgoing longwave radiation (OLR). LW scattering causes approximately 0.018 K/day cooling at the tropopause and about 0.028 K/day heating at the surface. Furthermore, over 40% of the total OLR bias for ice clouds is observed in 350-500 cm^{-1}. Overall, the radiative effects associated with neglecting LW scattering are comparable to the counterpart due to doubling atmospheric CO_2 under clear-sky conditions.

1. Introduction

Clouds cover approximately 67% of the globe according to observations made by the Moderate Resolution Imaging Spectrometer (MODIS) (King et al., 2013), and significantly affect the global energy budget (Baran, 2012; Hansen et al., 1997; Liou, 1986; Stephens, 2005; Stephens et al., 1990, 2001; Yang et al., 2015; Yi et al., 2013). If clouds absorb more longwave (LW) radiation from the surface and the lower part of the atmosphere than the LW energy they emit and the solar radiation they reflect to space, clouds retain energy in the atmosphere and warm the surface and the atmosphere. Conversely, clouds cool the earth-atmosphere system if they emit more LW radiation and reflect more solar radiation than the LW radiation they absorb.

Model approximations of radiative processes cause uncertainties in climate simulations. In the LW spectral bands, since cloud absorption dominates the extinction of radiation, fluxes are usually calculated by approximations that account for absorption only. However, several studies documented significant influences of scattering in LW radiative transfer. From GCM simulations, when LW scattering is included, Stephens et al. (2001) estimate that the global mean OLR decreases by 8 W/m^2, and Schmidt et al. (2006) state that OLR decreases by approximately 1.5 W/m^2 and increases surface downward flux by about 0.4 W/m^2. Using surface observations, Joseph and Min (2003) suggest that OLR is overestimated by as much as 6-8 W/m^2 due to neglecting LW scattering by thin cirrus clouds. By using the International Satellite Cloud Climatology Project (ISCCP) version D2 (Rossow & Schiffer, 1991) data, Costa and Shine (2006) estimate a 3 W/m^2 reduction in OLR from 60°S to 60°N due to light scattering.

According to those studies, estimates of the influence of LW light scattering by clouds on the global mean OLR range from 1.5 to 8 W/m^2. To estimate the effect of excluding LW scattering contributions, Costa and Shine (2006) suggest setting the scattering cross section to

zero, whereas Schmidt et al. (2006) recommend setting the asymmetry factor to unity. Although their approaches differ because they use different theories to account for LW scattering, both non-scattering simulations are performed by using cloud absorption rather than extinction optical thickness. Therefore, their estimated influences on the global mean OLR are similar. However, a 8 W/m^2 reduction on the global mean OLR estimated by Stephens et al. (2001) is larger than the estimates by Costa and Shine (2006) and Schmidt et al. (2006), and is similar to the largest evaluations in Joseph and Min (2003) by using ground observations when thin cirrus clouds are present. As mentioned by Costa and Shine (2006), the assessments in Stephens et al. (2001) are overestimated and the large overestimate is possibly caused by not considering cloud fractions in the simulations, because such a large influence occurs only under overcast conditions when high clouds exist.

Cloud information in the previous studies was from single ground observation site for ice clouds (Joseph & Min, 2003), GCM simulations (Schmidt et al., 2006; Stephens et al., 2001) or a climatological summary (Costa & Shine, 2006). These datasets are spatially coarse or may not provide realistic cloud top and base heights. With high spatial resolution cloud top and base heights now available from CALIPSO and CloudSat observations, we characterize the uncertainties of flux and heating rate simulations by using rigorous radiative transfer calculations combined with state-of-the-art cloud optics models to give an evaluation of climate effects based on the current level of understanding of cloud radiative properties. The remaining portion of this paper is organized as follows. The microphysical and bulk optical properties of clouds are described in section 2. In section 3, we outline the settings of the radiative transfer model (RTM) and the satellite data used in the simulations. Results and a discussion are given in section 4. Section 5 gives the conclusions of this study.

2. Cloud Microphysical and Optical Properties

This study uses the MODIS Collection 6 (MC6) cloud optics models (Platnick et al., 2015, 2017), which assume an ensemble of aggregates composed of 8 severely roughened columns for ice cloud particles and spheres for water cloud droplets. For the MC6 ice cloud model (Platnick et al., 2015, 2017), the single-scattering properties of individual ice particles are provided by an ice crystal library (Bi & Yang, 2017; Yang et al., 2013), including the extinction efficiency, single-scattering albedo, asymmetry parameter, phase function, and particle volume and projected area. The refractive index of ice applied in the library is from Warren and Brandt (2008). The library provides the optical properties of ice crystals for three degrees of roughness, namely, smooth, moderately rough, and severely rough. Roughened ice crystals are demonstrated from in-situ observations and satellite measurements, although the physical processes that cause the observed roughening are not well understood (Baum et al., 2011, 2014; Cole et al., 2013; Ding et al., 2016; Hioki, Yang, Baum, et al., 2016; Holz et al., 2016; Ulanowski et al., 2006, 2012). Furthermore, the treatment of forward scattering is improved to explicitly overcome the inadequacies of delta-transmission (Bi et al., 2009). Yang, Kattawar, et al. (2008) and Yang, Hong, et al. (2008) discuss the treatment of surface roughness of an ice particle and the resulting uncertainties in ice cloud property retrievals. The features of the ice cloud model include spectral consistency between MODIS-based solar and thermal retrievals (Baum et al., 2014) and better agreement of ice cloud optical thickness retrievals between the MODIS-based thermal method and CALIOP (Cloud Aerosol Lidar with Orthogonal Polarization) lidar ratios (Holz et al., 2016). For the MC6 water cloud model (Platnick et al., 2015, 2017), the Lorenz-Mie theory (Bohren & Huffman, 1998; van de Hulst, 1957) provides the single-scattering properties using the refractive index of water from compilations by Hale and Querry (1973) at wavelengths between 0.25 and

0.69 μm, Palmer and Williams (1974) at wavelengths between 0.69 and 2.0 μm, and Downing and Williams (1975) at wavelengths longer than 2.0 μm.

The effective diameter D_e (Baum, Heymsfield, et al., 2005; Baum et al., 2011, 2014; Foot, 1988) is defined to quantify the ensemble-averaged size of a population of irregular ice crystals as follows:

$$D_e = \frac{3\int_{D_{\min}}^{D_{\max}} V(D)N(D)dD}{2\int_{D_{\min}}^{D_{\max}} A(D)N(D)dD}, \quad (1)$$

where D is the maximum dimension of a particle, $D_{\max}$ and $D_{\min}$ are the largest and smallest particle maximum dimensions, $N(D)$ is the particle number concentration specified with respect to the maximum dimension D (cm^{-3} cm^{-1}), and V and A are the volume and the projected area of a particle. In the case of spherical particles, D_e reduces to the definition of the effective size in Hansen and Travis (1974). Therefore, we use D_e to consistently define the effective size of both water droplets and ice particles.

Given the optical properties and the particle size distributions (PSDs) of clouds, we average the single-scattering properties of the cloud model by the Planck function (B) at 233 K (Fu et al., 1998; Hong et al., 2009; Yi et al., 2013) in a specific spectral region to get band-averaged bulk-scattering properties (Baum, Yang, et al., 2005; Baum et al., 2011, 2014), such as

$$\bar{\sigma}_{ext/sca} = \frac{\int_{\lambda_1}^{\lambda_2}\int_{D_{\min}}^{D_{\max}} \sigma_{ext/sca}(D,\lambda)B(\lambda)N(D)dD\,d\lambda}{\int_{\lambda_1}^{\lambda_2}\int_{D_{\min}}^{D_{\max}} B(\lambda)N(D)dD\,d\lambda}, \quad (2)$$

$$\bar{Q}_{ext} = \frac{\int_{\lambda_1}^{\lambda_2}\int_{D_{min}}^{D_{max}} Q_{ext}(D,\lambda)A(D)B(\lambda)N(D)\,dD\,d\lambda}{\int_{\lambda_1}^{\lambda_2}\int_{D_{min}}^{D_{max}} A(D)B(\lambda)N(D)\,dD\,d\lambda}, \text{ and} \quad (3)$$

$$\bar{g} = \frac{\int_{\lambda_1}^{\lambda_2}\int_{D_{min}}^{D_{max}} g(D,\lambda)\sigma_{sca}(D,\lambda)B(\lambda)N(D)\,dD\,d\lambda}{\int_{\lambda_1}^{\lambda_2}\int_{D_{min}}^{D_{max}} \sigma_{sca}(D,\lambda)B(\lambda)N(D)\,dD\,d\lambda}, \quad (4)$$

where $\bar{\sigma}_{ext/sca}$, $\bar{Q}_{ext}$ and $\bar{g}$ are the band-averaged bulk extinction or scattering cross section, extinction efficiency and asymmetry factor, $\sigma_{ext/sca}$, Q_{ext} and g are the extinction or scattering cross section, the extinction efficiency and the asymmetry factor, and λ_1 and λ_2 are the lower and upper wavelength boundaries of a spectral band among those of the GCM version of the Longwave Rapid Radiative Transfer Model (RRTMG_LW, Clough et al., 2005; Iacono et al., 2008) listed in Table 1. The band-averaged bulk single-scattering albedo ($\bar{\omega}$) is defined as the ratio of the band-averaged bulk scattering and extinction cross section as follows:

$$\bar{\omega} = \frac{\bar{\sigma}_{sca}}{\bar{\sigma}_{ext}}. \quad (5)$$

For the MC6 cloud model, PSDs are modified gamma size distributions with an effective variance (Hansen & Travis, 1974) of 0.1 for both water and ice clouds (Platnick et al., 2015).

Figure 1 shows band-averaged $\bar{Q}_{ext}$, $\bar{\omega}$, and $\bar{g}$ from 10 to 3250 cm^{-1} for ice cloud particles with selected D_e values of 20 and 60 μm, and for water clouds with a selected droplet D_e of 20 μm. In general, $\bar{Q}_{ext}$ increases at first and then oscillates to approach the asymptotic value, 2, for large particles as the wavenumber increases, and water cloud droplets usually have larger values when compared to ice cloud particles with a similar size. For $\bar{g}$, ice clouds have more forward scattering than water clouds when particle sizes are about the same, and larger ice

particles have larger values than smaller particles. Since the imaginary part of the refractive index of ice is smaller than that of water between 250 and 750 cm^{-1}, and has a local minimum near 430 cm^{-1}, as shown in Figure 2, ϖ for ice clouds is larger than for water clouds in bands 1 to 5 (10-820 cm^{-1}), and has the largest value in band 2 (350-500 cm^{-1}). However, the imaginary part of the refractive index of water is smaller than that of ice between 1700 and 3000 cm^{-1}, leading to larger water clouds ϖ values in bands 12 to 16 (1800-3250 cm^{-1}).

3. Radiative Transfer Model Settings and Satellite Observations

Fluxes and heating rates are simulated by RRTMG_LW (Clough et al., 2005; Iacono et al., 2008) and the Discrete Ordinates Radiative Transfer (DISORT) Program for a Multi-Layered Plane-Parallel Medium (Stamnes et al., 1988). RRTMG_LW, which is a frequently used RTM in GCMs and numerical prediction models (Clough et al., 2005; Iacono et al., 2008), applies the correlated-k-distribution method (Lacis & Oinas, 1991) to account for atmospheric gas absorption, and divides the LW spectrum into the 16 intervals listed in Table 1, ranging from wavenumber 10 to 3250 cm^{-1}, in order to balance radiometric accuracy and computational efficiency (Clough et al., 2005; Iacono et al., 2000; Mlawer et al., 1997). In radiative transfer calculations, RRTMG_LW uses a two-stream model that angular resolution is low and only considers absorption. To rigorously investigate the possible influences of light scattering on flux and heating rate simulations containing clouds, we utilize the 16-stream DISORT (high angular resolution) as a radiative transfer solver, and implant the solver into RRTMG_LW. The optical thicknesses of the atmospheric profiles generated by RRTMG_LW, cloud profiles, and cloud optical properties are input into DISORT to simulate vertical distributions of fluxes and heating rates. The 16-stream DISORT computes fluxes with < 1% differences from an accurate 128-stream DISORT. All of the simulations in this study are offline, and computational time using

the 16-stream DISORT takes about 25 times longer than the original RRTMG_LW radiative transfer solver. To overcome the challenge associated with the strong forward peak of the cloud phase functions for radiative transfer simulation, we use the delta-M method (Hioki, Yang, Kattawar, et al., 2016; Wiscombe, 1977), which has been developed to ensure accurate flux computations by truncating the phase function and adjusting the optical thickness, single-scattering albedo, and Legendre polynomial expansion coefficients of the phase function based on the similarity principle (Liou, 2002; van de Hulst, 1974; Wiscombe, 1977).

The following satellite observation datasets are analyzed for 2010. The cloud conditions are provided by CCCM Edition B1 products (Kato et al., 2010, 2011, 2014), containing measurements derived from CALIPSO (resolution 333 m), CloudSat (resolution 1.4 km), CERES (resolution 20 km at the near-nadir view), and MODIS (resolution 1 km) observations. To merge cloud top and base heights in a 1 km grid box, three CALIPSO and one CloudSat observations are combined following Table 1 in Kato et al. (2010). The merged cloud heights are then collocated with 1 km MODIS observations, and are used as input in the enhanced cloud algorithm (Kato et al., 2011) to improve retrieved cloud optical and microphysical properties from MODIS observations. Then 1 km combined CALIPSO, CloudSat and MODIS data is collocated with CERES footprints to make the grid sizes of the CCCM products approximately 20 km (Kato et al., 2014). In a CCCM grid box, up to 16 unique cloud horizontal boundaries (groups) and up to 6 independent cloud vertical layers are sorted by a grouping process (Kato et al., 2010). Kato et al. (2011) show improvements of flux simulations by using these products, compared with CERES and surface measurements. In this study, we focus on single-layer water and ice clouds (water and ice cloud groups with a single cloud top and base) in 2010, and analyze the contribution of light scattering from different thermodynamic phases of clouds. From

the products, the cloud vertical boundaries are defined by the CALIPSO- and CloudSat-derived cloud top and base heights, and the cloud optical and microphysical properties are provided by the MODIS-retrieved cloud optical thickness, effective diameter, fraction and phase. Figure 3 presents histograms of the frequency of visible optical thickness and particle size for water and ice clouds. In 2010, both single-layer water and ice clouds most frequently have small optical thicknesses (< 5), and the most abundant particle sizes (D_e) are about 20 μm for water clouds and about 20 to 60 μm for ice clouds. With cloud top and base heights provided from CCCM products, we set the physical thickness of clouds and assume clouds are vertically homogeneous in the model simulations.

Atmospheric information, including temperature, humidity and ozone profiles, is provided by the CCCM products, based on the Goddard Earth Observing System (GEOS-5) Data Assimilation System reanalysis (Kato et al., 2014). The vertical range of atmospheric profiles in the simulations is from the surface to 65 km height. In order to simulate more realistic conditions, we follow the Fifth Assessment Report of the Intergovernmental Panel on Climate Change (IPCC, 2014) and set the volume mixing ratios of carbon dioxide (CO_2), nitrous oxide (N_2O), and methane (CH_4) to 390.5, 0.3242, and 1.803 ppmv, respectively.

4. Results and Discussion

To evaluate the consequences of ignoring light scattering in the LW spectrum by single-layer water and ice clouds, we compare fluxes and heating rates between absorption only and rigorous radiative transfer calculations including light scattering processes. Simulation biases are defined as the difference between calculations where only absorption is considered and more rigorous results that include scattering. Both calculations use the same RTM, which is a customized combination of RRTMG_LW and DISORT. In absorption-only simulations, as

suggested by Costa and Shine (2006), we use the absorption optical thicknesses of clouds and set the single-scattering albedo to zero, but the extinction optical thicknesses (i.e., scattering plus absorption optical thicknesses) and complete scattering properties are used in the rigorous calculations considering LW scattering. The absorption optical thicknesses of clouds are the same in these two sets of simulations.

The global impacts of ignoring LW scattering on flux and heating rate simulations are estimated by using cloud and atmosphere information from CCCM products covering 2010. To spatially represent the flux simulation biases, we average the biases into 1° × 1° resolution. Figure 4 shows the global annual mean bias distributions of upward flux at the TOA and of downward flux at the surface. The pattern of TOA upward flux biases is similar to that in Figure 6 in Costa and Shine (2006). In general, large biases can be found along the Intertropical Convergence Zone (ITCZ), particularly in the Pacific warm pool, and in the Tibetan Plateau region, where OLR is overestimated by up to about 12 W/m^2, since there are many ice clouds, which locate at higher altitudes with more transparent above-cloud atmospheric layers and have larger scatter properties as in Figure 1 than water clouds. In contrast, negative biases of downward flux at the surface are significant (about -3.6 W/m^2) in broad midlatitude regions and mountain areas, especially in the Tibetan Plateau, the Antarctic, and Greenland, because altitudes of these regions are higher and more scattered LW fluxes can reach the surface in a shorter path length without being absorbed by the atmosphere. Since water vapor absorbs most of the downward scattered fluxes, downward flux biases have smaller magnitudes than the upward flux biases. However, in a dry and high area under clouds, the downward scattered fluxes can reach the ground.

Zonal averaged flux and heating rate biases in each month of 2010 are shown in Figure 5. In Figure 5a, the peak TOA upward flux bias followed the ITCZ shifts from the southern to the northern hemisphere from January to June and shifts back again from July to December. From June to September, the contrast of biases between northern and southern hemispheres is largest. On the other hand, Figure 5b presents surface downward flux biases, which are mainly in the midlatitude region, as shown in Figure 4b. The surface downward flux biases are close to zero in the tropical regions due to absorption by abundant water vapor. Generally, as previously discussed, the absolute biases are larger for TOA upward flux than surface downward flux.

Figure 5c describes the net flux into the atmosphere (NF_A) (Zhang et al., 1995), which is defined as

$$NF_A = F_T^- - F_T^- - (F_S^- - F_S^-), \quad (6)$$

where F_T^- and F_T^- are downward and upward flux at the TOA, respectively, and F_S^- and F_S^- are downward and upward flux at the surface, respectively. When the simulations include LW scattering, clouds mainly scatter LW radiation from below and scatter back part of the energy to the ground, giving radiation more chance to be absorbed by the atmosphere, so the biases of net flux into the atmosphere are negative and extreme values vary with the positions of the ITCZ, such as in Figure 5a. In Figures 5d and 5e, heating rate biases are at the tropopause and at the surface, respectively. To evaluate simulation biases at the tropopause, we follow the method mentioned by Reichler et al. (2003) to determine the height of the tropopause. Since LW scattering decreases the amount of radiation reaching higher altitudes above the cloud layers, heating rate biases at the tropopause have similar monthly variations as in Figure 5a such that the locations of the largest absolute bias are in the southern hemisphere from January to March, in the northern hemisphere from April to November, and in the southern hemisphere again in

December. In Figure 5e, the largest surface heating rate biases are in the midlatitude areas, as anticipated from Figure 5b. Although the ITCZ is persistently cloudy, absolute heating rate biases at the surface are relatively small in this region, because downward scattered radiation is absorbed by water vapor before transferring to the surface.

Global annual averaged flux biases are depicted in Figure 6a and summarized in Table 2 with corresponding root mean square errors (RMSEs). Due to the optical properties (as in Figure 1) and altitudes of clouds, the global annual mean TOA upward flux bias for ice clouds (4.4 W/m^2) is larger than for water clouds (1.6 W/m^2). The annual mean downward flux bias at the surface is similar for ice (-1.3 W/m^2) and water (-1.1 W/m^2) clouds, since the atmosphere is opaque under cloud layers. In Figure 6a, the upward flux biases at the TOA are slightly smaller than at the tropopause for both water and ice clouds, because a fraction of the upward scattered fluxes are absorbed by the atmosphere above the tropopause. However, the downward flux biases at the tropopause are mainly from ice clouds, since most of water cloud layers are lower than the tropopause. When LW light scattering is considered, about 3.1 W/m^2 remains in the atmosphere when ice clouds exist, and for the existence of water clouds approximately 0.5 W/m^2 is remained in the atmosphere.

Averaging globally over water and ice clouds and neglecting LW scattering, upward flux at the TOA is overestimated by 2.6 W/m^2 and downward flux at the surface is underestimated by 1.2 W/m^2. The results are similar to the estimates in Costa and Shine (2006), which are 3 W/m^2 overestimation for TOA upward flux and 1.1 W/m^2 underestimation for surface downward flux from 60°S to 60°N. Globally, about 1.4 W/m^2 is absorbed in the atmosphere involving single-layer clouds and considering LW scattering. While the global mean flux biases are relatively small compared to the total TOA upward flux (233.8 W/m^2) and surface downward flux (351.9

W/m^2) from multi-sensor observations (Henderson et al., 2013), simulated biases are larger in some regions (Figure 4a), up to 9-12 W/m^2 over the ITCZ, or as much as 5% of total TOA upward flux. Compared to the LW cloud radiative effect of 27.2 W/m^2 at the TOA or 25.6 W/m^2 at the surface (Henderson et al., 2013), biases of TOA upward flux are about 10% and biases of surface downward flux are about 5% of LW cloud radiative effect.

Figure 6b shows global annual mean heating rate biases, and Table 3 lists the values and their respective RMSEs. Annual averaged biases are about -0.005 (< 1%), -0.042 (< 1%), 0.006 (< 1%), -0.034 (about 6.3%), 0.018 (about -3%), and -0.028 (about 2.3%) K/day, for the whole atmosphere column, in cloud layers, above cloud layers, under cloud layers, at the tropopause and at the surface, respectively. The values in the parentheses are percentage errors relative to heating rates for each layer. Since clouds mostly scatter back a fraction of upward radiation illuminating clouds from below to the ground, heating rate biases in and under cloud layers are negative, and above cloud layers are positive. Therefore, the global averaged magnitudes of column mean biases have relatively small values. Overall, scattered LW radiation is eventually absorbed in clouds, so the largest absolute heating rate biases are in the cloud layers. Although the absolute biases are large in the cloud layers, LW scattering causes relatively larger biases under cloud layers, at the tropopause and at the surface. In general, the magnitudes of heating rate biases are larger for ice clouds than for water clouds, especially at the tropopause where the RMSE is also largest.

To further demonstrate the importance of LW scattering, we compare the effect of neglecting LW scattering with the clear-sky radiative effect of doubling CO_2. As listed in Table 1 in Clough and Iacono (1995), when the concentration of CO_2 doubles from 355 to 710 ppmv under midlatitude summer conditions, upward fluxes at the TOA and tropopause decrease about

2.8 (2.6) and 3.9 (2.7) W/m^2, respectively, and downward fluxes at the surface and tropopause increase approximately 1.8 (1.2) and 1.7 (0.1) W/m^2, respectively, and cause heating about 0.069 (0.028) K/day at the surface and about 0.00002 (-0.018) K/day at the tropopause. The values in the parentheses are equivalent simulation biases listed in Tables 2 and 3. Overall, the simulation biases are comparable to the radiative effects of doubling CO_2.

Due to varying optical properties of clouds in each RRTMG_LW spectral band (Figure 1), the contributions of light scattering vary by bands, and the cumulative flux biases from 10 to 3250 cm^{-1} are shown in Figure 7. Since ice clouds have larger ϖ in the main LW emission bands (10-820 cm^{-1}, shown in Figure 1b) at Earth surface temperatures, flux biases of ice clouds are larger than for water clouds in those bands. Especially, as mentioned in section 2, ϖ is largest in band 2 (350-500 cm^{-1}) for ice clouds compared to water clouds, because the imaginary part of refractive index is relatively small for ice in that spectral range (Figure 2). Therefore, at the TOA, band 2 contributes over 40% of ice clouds flux biases, whereas band 2 only accounts for about 3% of water clouds flux biases. This confirms the implication in Chen et al. (2014) that ice clouds have a stronger scattering effect in far-infrared than in middle-infrared spectral regions. Although the ice cloud model is different, the simulations made by Edwards and Slingo (1996) also support the results that LW scattering is most important around 400 cm^{-1}.

In addition to the optical properties of clouds, gas absorption also plays an important role in spectral flux biases (Figure 7). Since the atmosphere is relatively transparent above clouds, the scattered upward fluxes can reach the TOA without being absorbed by gas, particularly by water vapor. As a result, the magnitudes of upward flux biases at the TOA are larger than the downward flux biases at the surface. However, for both water and ice clouds, the magnitudes of biases for upward flux at the TOA or downward flux at the surface are similar in bands 5 to 9

(700-1390 cm^{-1}). As those spectral regions are in the atmospheric window, scattered fluxes transfer through the spectrally transparent part of the atmosphere. In bands 10 to 16 (1390-3250 cm^{-1}), the intensities of scattered fluxes are small because of gas absorption, and a lack of LW emitted fluxes. Therefore, spectral flux biases are mainly contributed by far-infrared and the atmospheric window regions (10-1390 cm^{-1}).

As mentioned by Tselioudis et al. (2013), using CALIPSO and CloudSat, the cloud top and base height are detected and can be used to distinguish different cloud regimes. In this study, with the CALIPSO- and CloudSat-derived cloud top and base heights in the CCCM products, we separate 6 cloud regimes for cloud groups with a single cloud top and base, including HxMxL, HxM, MxL, 1H, 1M, and 1L, where 440 hPa separates high (H) and middle (M) clouds, and 680 hPa separates middle (M) and low (L) clouds. 1H, 1M, and 1L refer to single-layer high, middle, and low clouds, respectively; and HxMxL, HxM, and MxL denote continuous cloud layers from high to low, high to middle, and middle to low clouds, respectively.

Figure 8 presents flux and heating rate biases in the 6 cloud regimes. As the atmosphere above cloud layers are comparatively transparent, when LW scattering is neglected, TOA upward fluxes are overestimated by as much as 5 W/m^2 when high clouds (HxMxL, HxM, and 1H) exist, or up to 2.9 W/m^2 when the highest clouds are middle clouds (MxL and 1M), or 1.4 W/m^2 when only low clouds (1L) exist. Scattering effects are especially important for high clouds, since they account for approximately 58% of LW cloud radiative forcing at the TOA, as estimated by Hartmann et al. (1992). Due to gas absorptions below clouds, LW scattering adds about 1.4 W/m^2 to surface downward fluxes when clouds are present, except for 1H clouds (0.7 W/m^2). Overall, when light scattering is considered, high clouds absorb more LW radiation than low clouds. Particularly, HxMxL and 1H clouds accumulate about 4 W/m^2 in the atmosphere.

Similarly, the resulting heating rate biases are larger for high than low clouds, ranging from -0.014 K/day for 1H clouds to nearly zero for 1L clouds. In general, higher clouds have larger flux and heating rate biases.

Throughout the analyses, we notice that the values of RMSEs listed in Tables 2 and 3 are larger than the respective average biases. Since not only cloud microphysical and optical properties, as in Figures 1 and 3, but also cloud physical thicknesses and atmospheric conditions, vary around the globe, large biases can be found locally as in Figure 4. As a result, all RMSEs are considerably larger than the magnitudes of global mean biases.

5. Conclusions

To reduce the computational burden, an absorption approximation without considering scattering is a widely used method to deal with LW radiative transfer by clouds in GCMs and numerical weather prediction models. This study quantifies the flux and heating rate simulation biases caused by neglecting LW scattering.

To estimate the global average bias, we simulate global fluxes and heating rates in 2010 based on the CCCM merged satellite product. The previous study by Costa and Shine (2006) assumed a constant cloud physical thickness as a function of the cloud top height. Since the CCCM product contains cloud top and base heights from CALIPSO and CloudSat observations (Kato et al., 2014), the cloud thickness is adjusted based on the satellite observations. Because ice clouds are most abundant over the ITCZ, significant overestimation of TOA upward flux (~12 W/m^2) can occur by neglecting scattering, especially in the Pacific warm pool. However, surface downward flux biases are largest mainly in midlatitude, polar, and mountain areas, with regional peak underestimation by neglecting scattering about 3.6 W/m^2 in Tibetan Plateau, Antarctic, and Greenland areas.

In the temporal domain, the locations of extreme zonally averaged biases vary with the ITCZ over 12 months. The peak value shifts from the southern to the northern hemisphere from January to June and then shifts back to southern hemisphere from July to December. As a global average, when neglecting LW scattering in clouds, OLR is overestimated by 2.6 W/m^2, and downward flux at the surface is underestimated by 1.2 W/m^2. Therefore, when we include the scattering effect of clouds in simulations based on the atmosphere and cloud conditions in a specific moment of a satellite observation, 1.4 W/m^2 is retained in the atmosphere. The TOA upward and surface downward flux biases are about 10% and 5%, respectively, of the global LW cloud radiative effect, which are approximately 27.2 W/m^2 at the TOA and 25.6 W/m^2 at the surface (Henderson et al., 2013). Although compared to global annual averaged OLR about 233.8 W/m^2 (Henderson et al., 2013), the flux bias of 2.6 W/m^2 at the TOA is not large, the regional biases are more significant, up to 9 to 12 W/m^2 at the TOA over the ITCZ, or about 5% of global averaged OLR at most. By neglecting scattering, annual tropopause heating rate biases are about 0.018 K/day, which is -3% of the annually averaged heating rate at that level, and annual heating rate biases at the surface are approximately -0.028 K/day or 2.3% of the surface annual mean heating rate. After comparing with flux and heating rate simulations, we find that the influence of doubling CO_2 (Clough & Iacono, 1995) and LW scattering are similar. Consequently, scattering in the LW spectrum is important and has to be considered in model simulations.

Due to distinct optical properties of clouds in the RRTMG_LW 16 spectral bands, ice clouds have larger flux biases than water clouds in 10-820 cm^{-1}. The biases of TOA upward flux and surface downward flux are similar in 700-1390 cm^{-1}, because they are in the atmospheric window region. Overall, nearly all of the flux biases are in far-infrared and the atmospheric

window regions (10-1390 cm^{-1}). Among them, the upward flux bias at the TOA for ice clouds in band 2 (350-500 cm^{-1}) is largest, contributing over 40% of the total ice cloud bias, because there is a local minimum near 430 cm^{-1} in the imaginary part of the ice refractive index.

Generally, biases are larger for ice clouds than water clouds, and are larger for higher and thicker clouds. For ice clouds, the annual mean TOA upward flux bias and the annual mean surface downward flux bias are about 4.4 and -1.3 W/m^2, respectively, and for water clouds are about 1.6 and -1.1 W/m^2, respectively. The thickest high-top clouds (denoted HxMxL and HxM) have the largest biases, where OLR can be overestimated by up to 5 W/m^2 and downward flux at the surface can be underestimated by up to 1.4 W/m^2.

In conclusion, when LW scattering is neglected, an annual global averaged overestimation of 2.6 W/m^2 in OLR in this study is between 3 W/m^2 estimated by Costa and Shine (2006) and 1.5 W/m^2 by Schmidt et al. (2006), and is much less than 8 W/m^2 by Stephens et al. (2001). The present study uses rigorous radiative transfer calculations in flux and heating rate simulations, including the advanced MC6 cloud optics models, high spatial resolution CCCM merged satellite products, and observed physical cloud thicknesses. Consequently, global and regional circulation models have to take LW scattering of clouds into account to simulate realistic radiation fields, especially in the far-infrared spectral region with ice clouds.

Acknowledgments

Funding of the work is supported by the U.S. Department of Energy (DOE) Grant DE-SC0013080. E. Mlawer and P. Yang also acknowledge support from the U.S. National Science Foundation (AGS-1632209). The simulations in the study were performed using resources from the Texas A&M Supercomputing Facility (http://sc.tamu.edu). The RRTMG_LW code can be accessed freely through the Atmospheric and Environmental Research (AER) webpage

(http://rtweb.aer.com/main.html). The CCCM products are publicly available from the Atmospheric Science Data Center (ASDC) at NASA Langley Research Center (https://eosweb.larc.nasa.gov/).

References

Baran, A. J. (2012). From the single-scattering properties of ice crystals to climate prediction: A way forward. *Atmospheric Research*, *112*, 45–69. doi:10.1016/j.atmosres.2012.04.010

Baum, B. A., Heymsfield, A. J., Yang, P., & Bedka, S. T. (2005). Bulk scattering properties for the remote sensing of ice clouds. Part I: Microphysical data and models. *Journal of Applied Meteorology*, *44*(12), 1885–1895. doi:10.1175/JAM2308.1

Baum, B. A., Yang, P., Heymsfield, A. J., Platnick, S., King, M. D., Hu, Y.-X., & Bedka, S. T. (2005). Bulk scattering properties for the remote sensing of ice clouds. Part II: Narrowband models. *Journal of Applied Meteorology*, *44*(12), 1896–1911. doi:10.1175/JAM2309.1

Baum, B. A., Yang, P., Heymsfield, A. J., Schmitt, C. G., Xie, Y., Bansemer, A., … Zhang, Z. (2011). Improvements in shortwave bulk scattering and absorption models for the remote sensing of ice clouds. *Journal of Applied Meteorology and Climatology*, *50*(5), 1037–1056. doi:10.1175/2010JAMC2608.1

Baum, B. A., Yang, P., Heymsfield, A. J., Bansemer, A., Cole, B. H., Merrelli, A., … Wang, C. (2014). Ice cloud single-scattering property models with the full phase matrix at wavelengths from 0.2 to 100 μm. *Journal of Quantitative Spectroscopy and Radiative Transfer*, *146*, 123–139. doi:10.1016/j.jqsrt.2014.02.029

Bi, L., & Yang, P. (2017). Improved ice particle optical property simulations in the ultraviolet to far-infrared regime. *Journal of Quantitative Spectroscopy and Radiative Transfer*, *189*, 228–237. doi:10.1016/j.jqsrt.2016.12.007

Bi, L., Yang, P., Kattawar, G. W., Baum, B. A., Hu, Y. X., Winker, D. M., … Lu, J. Q. (2009). Simulation of the color ratio associated with the backscattering of radiation by ice particles at the

wavelengths of 0.532 and 1.064 μm. *Journal of Geophysical Research*, *114*(D4), D00H08. doi:10.1029/2009JD011759

Bohren, C. F., & Huffman, D. R. (1998). *Absorption and Scattering of Light by Small Particles*. New York: Wiley. doi:10.1002/9783527618156

Chen, X.H., Huang, X.L., & Flanner, M. G. (2014). Sensitivity of modeled far-IR radiation budgets in polar continents to treatments of snow surface and ice cloud radiative properties. *Geophysical Research Letters*, *41*(18), 799–804. doi:10.1002/2014GL061216

Clough, S. A., & Iacono, M. J. (1995). Line-by-line calculation of atmospheric fluxes and cooling rates: 2. Application to carbon dioxide, ozone, methane, nitrous oxide and the halocarbons. *Journal of Geophysical Research*, *100*(D8), 16519–16535. doi:10.1029/95JD01386

Clough, S. A., Shephard, M. W., Mlawer, E. J., Delamere, J. S., Iacono, M. J., Cady-Pereira, K., … Brown, P. D. (2005). Atmospheric radiative transfer modeling: A summary of the AER codes. *Journal of Quantitative Spectroscopy and Radiative Transfer*, *91*(2), 233–244. doi:10.1016/j.jqsrt.2004.05.058

Cole, B. H., Yang, P., Baum, B. A., Riedi, J., C.-Labonnote, L., Thieuleux, F., & Platnick, S. (2013). Comparison of PARASOL observations with polarized reflectances simulated using different ice habit mixtures. *Journal of Applied Meteorology and Climatology*, *52*(1), 186–196. doi:10.1175/JAMC-D-12-097.1

Costa, S. M. S., & Shine, K. P. (2006). An estimate of the global impact of multiple scattering by clouds on outgoing long-wave radiation. *Quarterly Journal of the Royal Meteorological Society*, *132*(616), 885–895. doi:10.1256/qj.05.169

Ding, J., Yang, P., Holz, R. E., Platnick, S., Meyer, K. G., Vaughan, M. A., … King, M. D. (2016). Ice cloud backscatter study and comparison with CALIPSO and MODIS satellite data. *Optics Express*, *24*(1), 620–636. doi:10.1364/OE.24.000620

Downing, H. D., & Williams, D. (1975). Optical constants of water in the infrared. *Journal of Geophysical Research*, *80*(12), 1656–1661. doi:10.1029/JC080i012p01656

Edwards, J. M., & Slingo, A. (1996). Studies with a flexible new radiation code. I: Choosing a configuration for a large-scale model. *Quarterly Journal of the Royal Meteorological Society*, *122*(531), 689–719. doi:10.1002/qj.49712253107

Foot, J. S. (1988). Some observations of the optical properties of clouds. II: Cirrus. *Quarterly Journal of the Royal Meteorological Society*, *114*(479), 145–164. doi:10.1002/qj.49711447908

Fu, Q., Yang, P., & Sun, W. B. (1998). An accurate parameterization of the infrared radiative properties of cirrus clouds for climate models. *Journal of Climate, 11*(9), 2223–2237. doi:10.1175/1520-0442(1998)011<2223:AAPOTI>2.0.CO;2

Hale, G. M., & Querry, M. R. (1973). Optical constants of water in the 200-nm to 200-μm wavelength region. *Applied Optics*, *12*(3), 555–563. doi:10.1364/AO.12.000555

Hansen, J. E., & Travis, L. D. (1974). Light scattering in planetary atmospheres. *Space Science Reviews*, *16*(4), 527–610. doi:10.1007/BF00168069

Hansen, J., Sato, M., & Ruedy, R. (1997). Radiative forcing and climate response. *Journal of Geophysical Research: Atmospheres*, *102*(D6), 6831–6864. doi:10.1029/96JD03436

Hartmann, D. L., Ockert-Bell, M. E., & Michelsen, M. L. (1992). The effect of cloud type on Earth's energy balance: Global analysis. *Journal of Climate*, *5*(11), 1281–1304. doi:10.1175/1520-0442(1992)005<1281:TEOCTO>2.0.CO;2

Henderson, D. S., L'Ecuyer, T., Stephens, G., Partain, P., & Sekiguchi, M. (2013). A multisensor perspective on the radiative impacts of clouds and aerosols. *Journal of Applied Meteorology and Climatology, 52*(4), 853–871. doi:10.1175/JAMC-D-12-025.1

Hioki, S., Yang, P., Baum, B. A., Platnick, S., Meyer, K. G., King, M. D., & Riedi, J. (2016). Degree of ice particle surface roughness inferred from polarimetric observations. *Atmospheric Chemistry and Physics, 16*(12), 7545–7558. doi:10.5194/acp-16-7545-2016

Hioki, S., Yang, P., Kattawar, G. W., & Hu, Y. (2016). Truncation of the scattering phase matrix for vector radiative transfer simulation. *Journal of Quantitative Spectroscopy and Radiative Transfer, 183*, 70–77. doi:10.1016/j.jqsrt.2016.06.011

Holz, R. E., Platnick, S., Meyer, K., Vaughan, M., Heidinger, A., Yang, P., … Wang, C. (2016). Resolving ice cloud optical thickness biases between CALIOP and MODIS using infrared retrievals. *Atmospheric Chemistry and Physics*, *16*(8), 5075–5090. doi:10.5194/acp-16-5075-2016

Hong, G., Yang, P., Baum, B. A., Heymsfield, A. J., & Xu, K.-M. (2009). Parameterization of shortwave and longwave radiative properties of ice clouds for use in climate models. *Journal of Climate, 22*(23), 6287–6312. doi:10.1175/2009JCLI2844.1

Iacono, M. J., Mlawer, E. J., Clough, S. A., & Morcrette, J.-J. (2000). Impact of an improved longwave radiation model, RRTM, on the energy budget and thermodynamic properties of the NCAR community climate model, CCM3. *Journal of Geophysical Research: Atmospheres*, *105*(D11), 14873–14890. doi:10.1029/2000JD900091

Iacono, M. J., Delamere, J. S., Mlawer, E. J., Shephard, M. W., Clough, S. A., & Collins, W. D. (2008). Radiative forcing by long-lived greenhouse gases: Calculations with the AER radiative transfer

models. *Journal of Geophysical Research: Atmospheres*, *113*(13), 2–9. doi:10.1029/2008JD009944

IPCC (2014). *Climate Change 2013: The Physical Science Basis. Contribution of Working Group I to the Fifth Assessment Report of the Intergovernmental Panel on Climate Change*. (T. F. Stocker, D. Qin, G.-K. Plattner, M. Tignor, S. K. Allen, J. Boschung, … P. M. Midgley, Eds.). Cambridge, NY: Cambridge University Press. doi:10.1017/CBO9781107415324

Joseph, E., & Min, Q. (2003). Assessment of multiple scattering and horizontal inhomogeneity in IR radiative transfer calculations of observed thin cirrus clouds. *Journal of Geophysical Research: Atmospheres*, *108*(D13), 4380. doi:10.1029/2002JD002831

Kato, S., Sun-Mack, S., Miller, W. F., Rose, F. G., Chen, Y., Minnis, P., & Wielicki, B. A. (2010). Relationships among cloud occurrence frequency, overlap, and effective thickness derived from CALIPSO and CloudSat merged cloud vertical profiles. *Journal of Geophysical Research*, *115*(D4), D00H28. doi:10.1029/2009JD012277

Kato, S., Rose, F. G., Sun-Mack, S., Miller, W. F., Chen, Y., Rutan, D. A., … Collins, W. D. (2011). Improvements of top-of-atmosphere and surface irradiance computations with CALIPSO-, CloudSat-, and MODIS-derived cloud and aerosol properties. *Journal of Geophysical Research*, *116*(D19), D19209. doi:10.1029/2011JD016050

Kato, S., Miller, W. F., Sun-Mack, S., Rose, F. G., Chen, Y., & Mlynczak, P. E. (2014). Variable descriptions of the A-train integrated CALIPSO, CloudSat, CERES, and MODIS merged product (CCCM or C3M), Version RelB1.v2. Retrieved from https://eosweb.larc.nasa.gov/project/ceres/readme/c3m_variables_B1_v2.pdf

King, M. D., Platnick, S., Menzel, W. P., Ackerman, S. A., & Hubanks, P. A. (2013). Spatial and temporal distribution of clouds observed by MODIS onboard the Terra and Aqua satellites. *IEEE*

Transactions on Geoscience and Remote Sensing, *51*(7), 3826–3852. doi:10.1109/TGRS.2012.2227333

Lacis, A. A., & Oinas, V. (1991). A description of the correlated k distribution method for modeling nongray gaseous absorption, thermal emission, and multiple scattering in vertically inhomogeneous atmospheres. *Journal of Geophysical Research*, *96*(D5), 9027–9063. doi:10.1029/90JD01945

Liou, K.-N. (1986). Influence of cirrus clouds on weather and climate processes: A global perspective. *Monthly Weather Review*, *114*(6), 1167–1199. doi:10.1175/1520-0493(1986)114<1167:IOCCOW>2.0.CO;2

Liou, K.-N. (2002). *An Introduction to Atmospheric Radiation (2nd ed.)*. Amsterdam ; Boston: Academic Press.

Mlawer, E. J., Taubman, S. J., Brown, P. D., Iacono, M. J., & Clough, S. A. (1997). Radiative transfer for inhomogeneous atmospheres: RRTM, a validated correlated-k model for the longwave. *Journal of Geophysical Research*, *102*(D14), 16663–16682. doi:10.1029/97JD00237

Palmer, K. F., & Williams, D. (1974). Optical properties of water in the near infrared. *Journal of the Optical Society of America*, *64*(8), 1107–1110. doi:10.1364/JOSA.64.001107

Platnick, S., King, M. D., Meyer, K. G., Wind, G., Amarasinghe, N., Marchant, B., … Riedi, J. (2015). MODIS cloud optical properties: User guide for the Collection 6 Level-2 MOD06/MYD06 product and associated Level-3 Datasets, Version 1.0. Retrieved from http://modis-atmos.gsfc.nasa.gov/_docs/C6MOD06OPUserGuide.pdf

Platnick, S., Meyer, K. G., King, M. D., Wind, G., Amarasinghe, N., Marchant, B., … Riedi, J. (2017). The MODIS cloud optical and microphysical products: Collection 6 updates and examples from

Terra and Aqua. *IEEE Transactions on Geoscience and Remote Sensing*, *55*(1), 502–525. doi:10.1109/TGRS.2016.2610522

Reichler, T., Dameris, M., & Sausen, R. (2003). Determining the tropopause height from gridded data. *Geophysical Research Letters*, *30*(20). doi:10.1029/2003GL018240

Rossow, W. B., & Schiffer, R. A. (1991). ISCCP cloud data products. *Bulletin of the American Meteorological Society*, *72*(1), 2–20. doi:10.1175/1520-0477(1991)072<0002:ICDP>2.0.CO;2

Schmidt, G. A., Ruedy, R., Hansen, J. E., Aleinov, I., Bell, N., Bauer, M., … Yao, M.-S. (2006). Present-day atmospheric simulations using GISS ModelE: Comparison to in situ, satellite, and reanalysis data. *Journal of Climate*, *19*(2), 153–192. doi:10.1175/JCLI3612.1

Stamnes, K., Tsay, S.-C., Wiscombe, W., & Jayaweera, K. (1988). Numerically stable algorithm for discrete-ordinate-method radiative transfer in multiple scattering and emitting layered media. *Applied Optics*, *27*(12), 2502–2509. doi:10.1364/AO.27.002502

Stephens, G. L. (2005). Cloud feedbacks in the climate system: A critical review. *Journal of Climate*, *18*(2), 237–273. doi:10.1175/JCLI-3243.1

Stephens, G. L., Tsay, S.-C., Stackhouse, P. W., & Flatau, P. J. (1990). The relevance of the microphysical and radiative properties of cirrus clouds to climate and climatic feedback. *Journal of the Atmospheric Science*s, *47*(14), 1742–1754. doi:10.1175/1520-0469(1990)047<1742:TROTMA>2.0.CO;2

Stephens, G. L., Gabriel, P. M., & Partain, P. T. (2001). Parameterization of atmospheric radiative transfer. Part I: Validity of simple models. *Journal of the Atmospheric Sciences*, *58*(22), 3391–3409. doi:10.1175/1520-0469(2001)058<3391:POARTP>2.0.CO;2

Tselioudis, G., Rossow, W., Zhang, Y., & Konsta, D. (2013). Global weather states and their properties from passive and active satellite cloud retrievals. *Journal of Climate*, *26*(19), 7734–7746. doi:10.1175/JCLI-D-13-00024.1

Ulanowski, Z., Hesse, E., Kaye, P. H., & Baran, A. J. (2006). Light scattering by complex ice-analogue crystals. *Journal of Quantitative Spectroscopy and Radiative Transfer*, *100*(1–3), 382–392. doi:10.1016/j.jqsrt.2005.11.052

Ulanowski, Z., Hirst, E., Kaye, P. H., & Greenaway, R. (2012). Retrieving the size of particles with rough and complex surfaces from two-dimensional scattering patterns. *Journal of Quantitative Spectroscopy and Radiative Transfer*, *113*(18), 2457–2464. doi:10.1016/j.jqsrt.2012.06.019

van de Hulst, H. C. (1957). *Light Scattering by Small Particles*. New York: Wiley.

van de Hulst, H. C. (1974). The spherical albedo of a planet covered with a homogeneous cloud layer. *Astronomy and Astrophysics*, *35*(2), 209–214.

Warren, S. G., & Brandt, R. E. (2008). Optical constants of ice from the ultraviolet to the microwave: A revised compilation. *Journal of Geophysical Research: Atmospheres*, *113*(14), 1–10. doi:10.1029/2007JD009744

Wiscombe, W. J. (1977). The delta–M method: Rapid yet accurate radiative flux calculations for strongly asymmetric phase functions. *Journal of the Atmospheric Sciences*, *34*(9), 1408–1422. doi:10.1175/1520-0469(1977)034<1408:TDMRYA>2.0.CO;2

Yang, P., Kattawar, G. W., Hong, G., Minnis, P., & Hu, Y. (2008). Uncertainties associated with the surface texture of ice particles in satellite-based retrieval of cirrus clouds—Part I: Single-scattering properties of ice crystals with surface roughness. *IEEE Transactions on Geoscience and Remote Sensing*, *46*(7), 1940–1947. doi:10.1109/TGRS.2008.916471

Yang, P., Hong, G., Kattawar, G. W., Minnis, P., & Hu, Y. (2008). Uncertainties associated with the surface texture of ice particles in satellite-based retrieval of cirrus clouds: Part II—Effect of particle surface roughness on retrieved cloud optical thickness and effective particle size. *IEEE Transactions on Geoscience and Remote Sensing*, *46*(7), 1948–1957. doi:10.1109/TGRS.2008.916472

Yang, P., Bi, L., Baum, B. A., Liou, K.-N., Kattawar, G. W., Mishchenko, M. I., & Cole, B. (2013). Spectrally consistent scattering, absorption, and polarization properties of atmospheric ice crystals at wavelengths from 0.2 to 100 μm. *Journal of the Atmospheric Sciences*, *70*(1), 330–347. doi:10.1175/JAS-D-12-039.1

Yang, P., Liou, K., Bi, L., Liu, C., Yi, B., & Baum, B. A. (2015). On the radiative properties of ice clouds: Light scattering, remote sensing, and radiation parameterization. *Advances in Atmospheric Sciences*, *32*(1), 32–63. doi:10.1007/s00376-014-0011-z

Yi, B., Yang, P., Baum, B. A., L'Ecuyer, T., Oreopoulos, L., Mlawer, E. J., … Liou, K.-N. (2013). Influence of ice particle surface roughening on the global cloud radiative effect. *Journal of the Atmospheric Sciences*, *70*(9), 2794–2807. doi:10.1175/JAS-D-13-020.1

Zhang, Y.-C., Rossow, W. B., & Lacis, A. A. (1995). Calculation of surface and top of atmosphere radiative fluxes from physical quantities based on ISCCP data sets: 1. Method and sensitivity to input data uncertainties. *Journal of Geophysical Research: Atmospheres*, *100*(D1), 1149–1165. doi:10.1029/94JD02747

Table 1. RRTMG_LW spectral band intervals.

Band	Wavenumber (cm^{-1})
1	10-350
2	350-500
3	500-630
4	630-700
5	700-820
6	820-980
7	980-1080
8	1080-1180
9	1180-1390
10	1390-1480
11	1480-1800
12	1800-2080
13	2080-2250
14	2250-2380
15	2380-2600
16	2600-3250

Table 2. 2010 global and annual mean biases and respective RMSEs for upward flux at the TOA and at the tropopause, downward flux at the tropopause and at the surface, and net flux into the atmosphere for total clouds, ice clouds, and water clouds.

	Unit (W/m^2)	Total Clouds	Ice Clouds	Water Clouds
Upward Flux (TOA)	Bias	2.6	4.4	1.6
	RMSE	3.6	5.3	1.8
Upward Flux (Tropopause)	Bias	2.7	4.4	1.6
	RMSE	3.6	5.4	1.9
Downward Flux (Tropopause)	Bias	-0.1	-0.2	-0.004
	RMSE	0.5	0.8	0.1
Downward Flux (Surface)	Bias	-1.2	-1.3	-1.1
	RMSE	1.6	1.8	1.4
NF_A	Bias	-1.4	-3.1	-0.5
	RMSE	2.7	4.1	1.0

Table 3. 2010 global annual mean biases and respective RMSEs of column mean, cloud layer mean, above cloud layer mean, under cloud layer mean, tropopause, and surface heating rate biases for total clouds, ice clouds, and water clouds. Column, cloud, above cloud, and under cloud heating rate biases indicate averaged heating rate biases over the whole atmospheric profile, in cloud layers, in layers above clouds, and in layers under clouds, respectively.

	Unit (K/day)	Total Clouds	Ice Clouds	Water Clouds
Column	Bias	-0.005	-0.010	-0.001
	RMSE	0.010	0.014	0.005
Cloud	Bias	-0.042	-0.034	-0.047
	RMSE	0.102	0.074	0.116
Above Cloud	Bias	0.006	0.008	0.005
	RMSE	0.008	0.010	0.006
Under Cloud	Bias	-0.034	-0.041	-0.030
	RMSE	0.044	0.053	0.037
Tropopause	Bias	0.018	0.044	0.002
	RMSE	0.126	0.200	0.033
Surface	Bias	-0.028	-0.026	-0.029
	RMSE	0.046	0.041	0.048

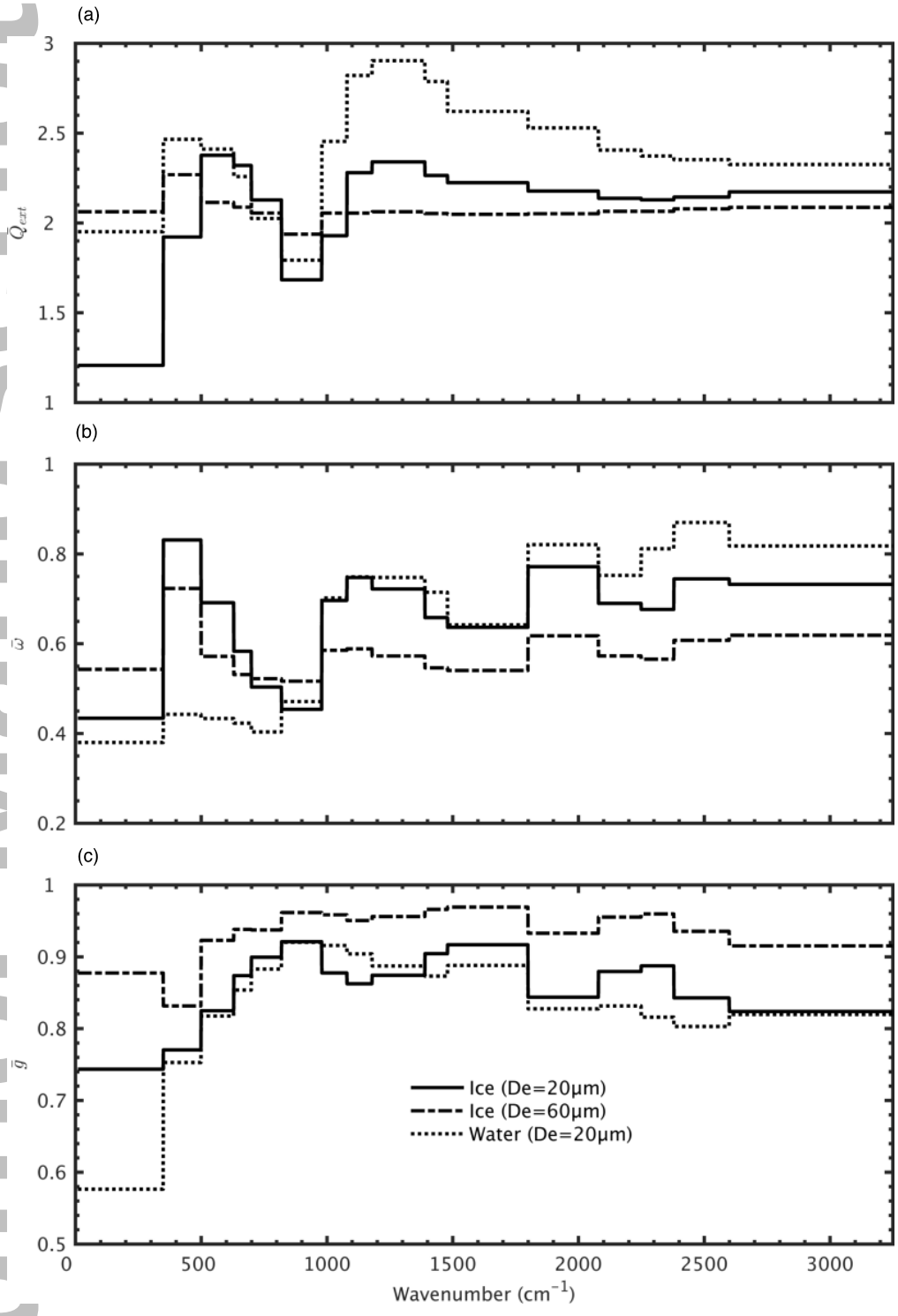

Figure 1. Band-averaged (a) bulk extinction efficiency, (b) single-scattering albedo, and (c) asymmetry factor from 10 to 3250 cm^{-1}. Solid and dash-dotted lines are for ice particles with 20 and 60 μm D_e, respectively; dotted lines are for water cloud droplets with 20 μm D_e.

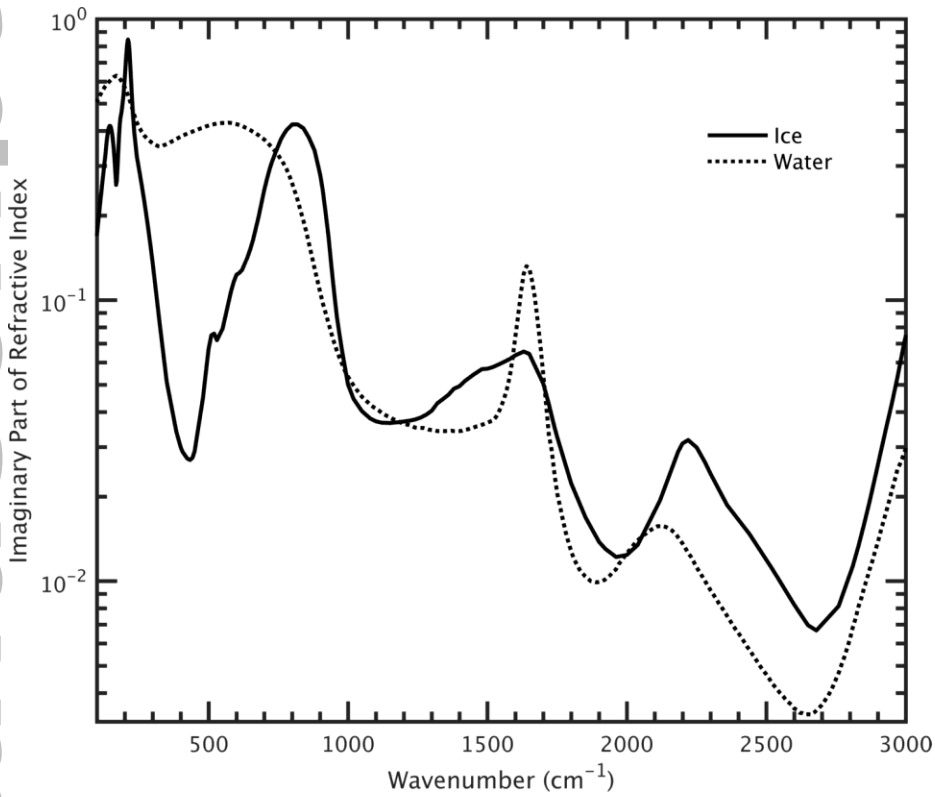

Figure 2. Imaginary part of refractive index of (solid line) ice and (dotted line) water cloud from 100 to 3000 cm^{-1}. The refractive index of ice are from Warren and Brandt (2008), and the refractive index of water are combined from Hale and Querry (1973), Palmer and Williams (1974), and Downing and Williams (1975).

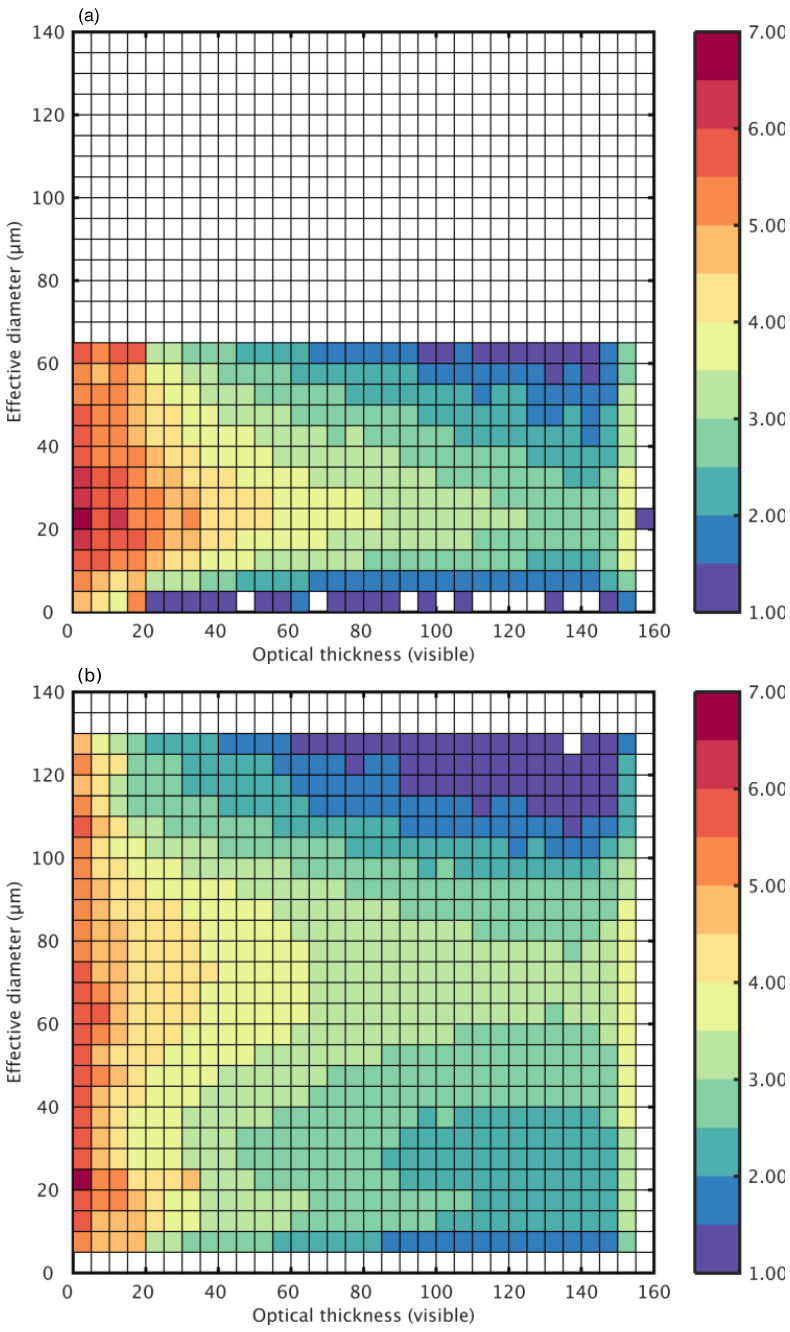

Figure 3. Two-dimensional histograms of the number of CCCM merged observations in 2010 in visible optical thickness and particle size bins for single-layer (a) water and (b) ice clouds (water and ice cloud groups with a single cloud top and base). Color bar shows the number of counts in a log scale (10^x).

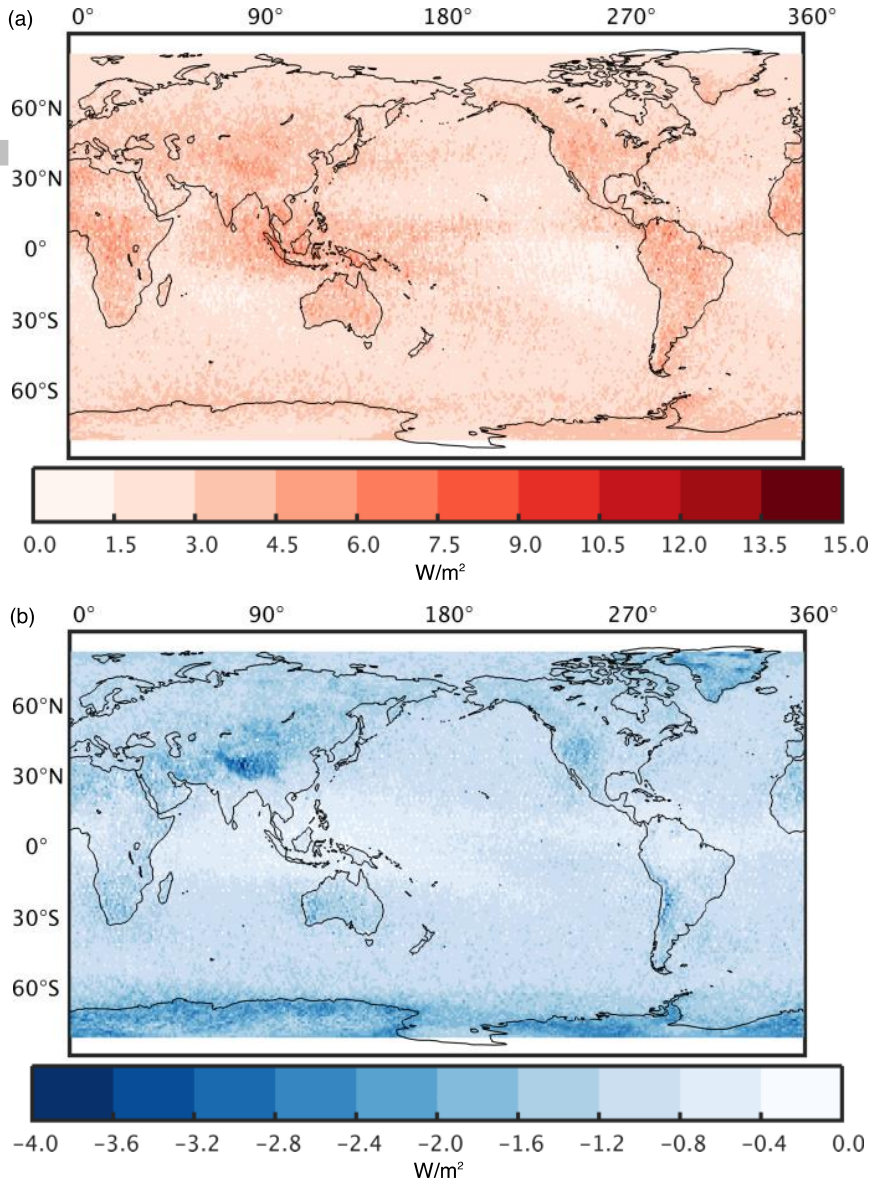

Figure 4. Global distributions (1° × 1°) of the annual mean LW biases in 2010 for (a) the upward flux at the TOA and (b) the downward flux at the surface. Blank regions indicate no satellite observations.

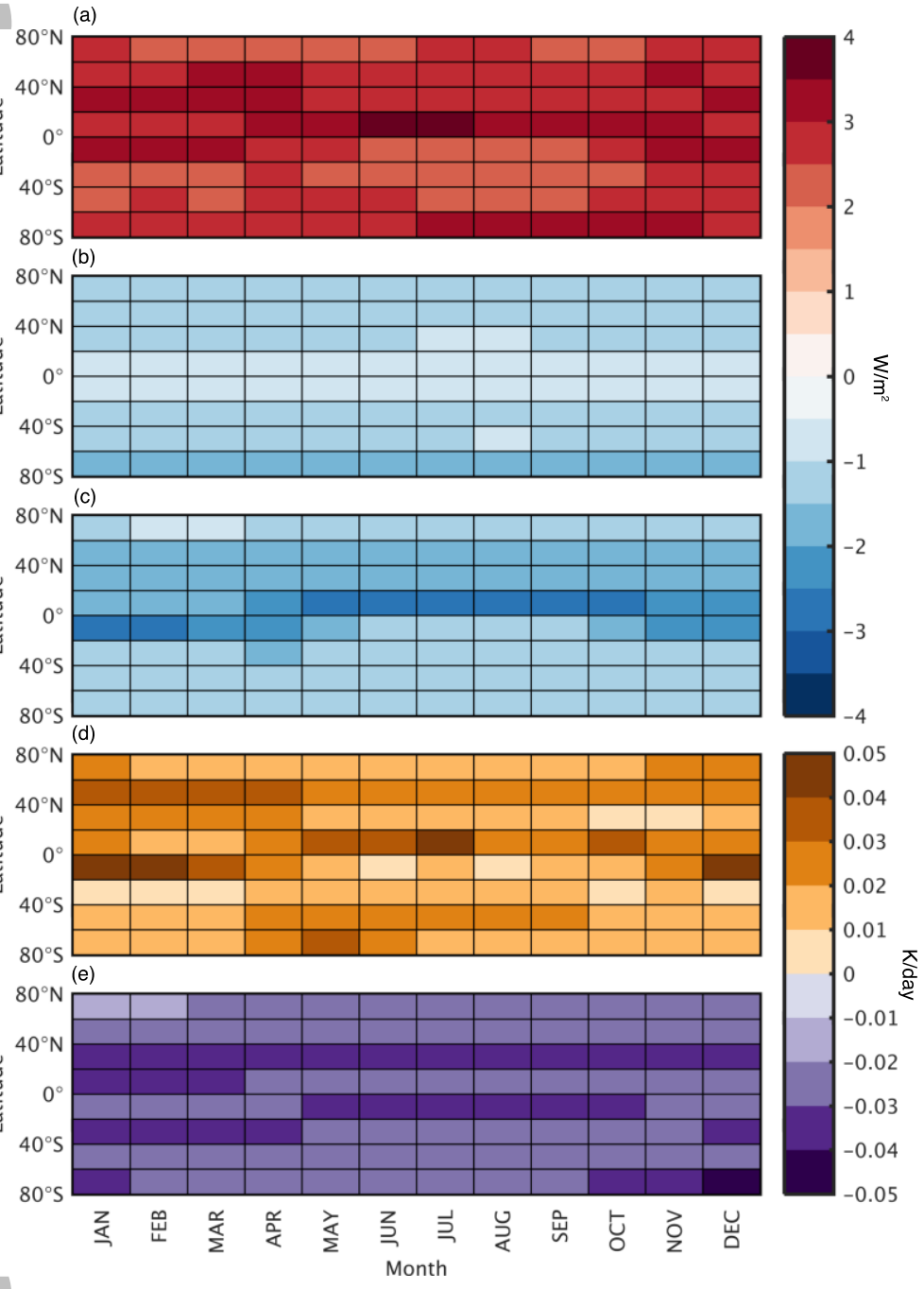

Figure 5. Monthly zonal mean LW biases in 2010 of (a) the upward flux at the TOA, (b) the downward flux at the surface, (c) the net flux into the atmosphere, (d) the heating rate at the tropopause, and (e) the heating rate at the surface.

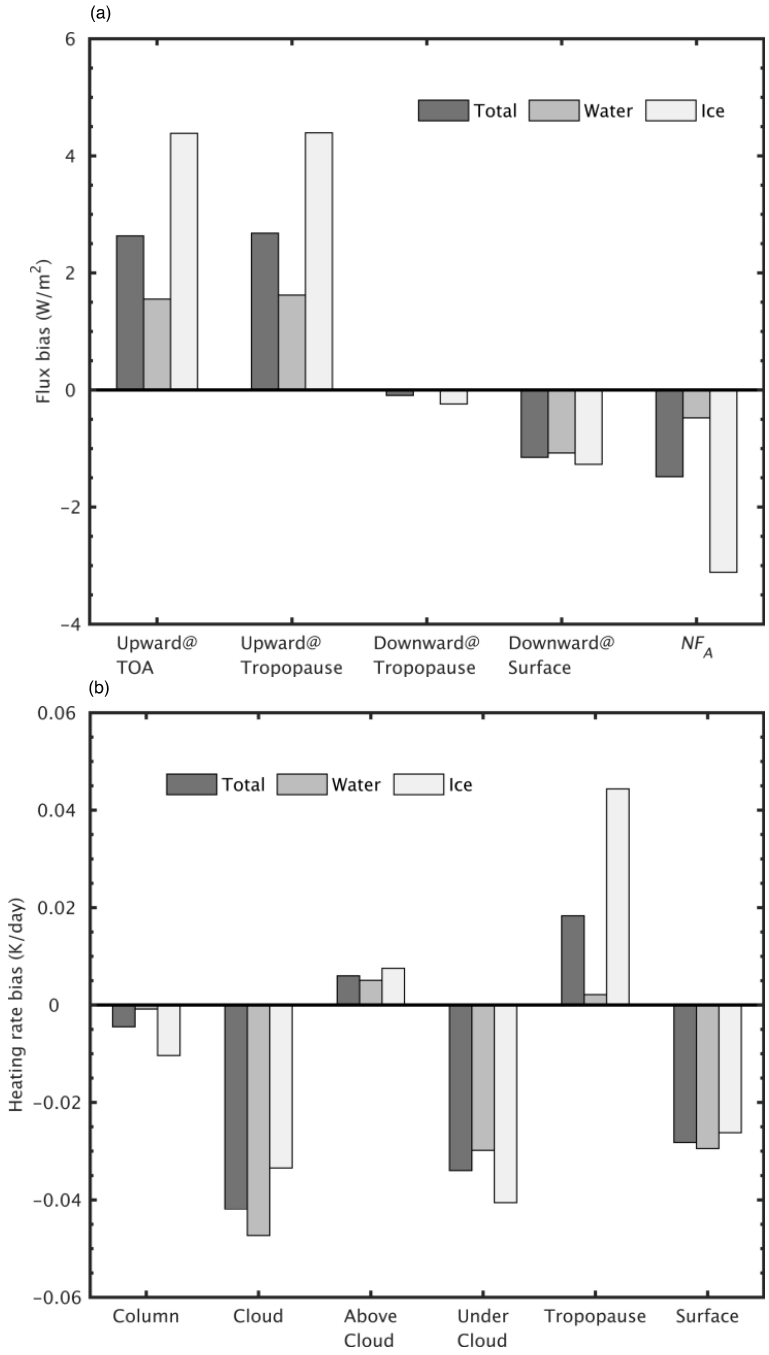

Figure 6. Annual global mean LW biases in 2010 of (a) the upward flux at the TOA and the tropopause, the downward flux at the tropopause and the surface, and the net flux into the atmosphere, and (b) the mean heating rate biases through the whole atmosphere column, in cloud layers, above cloud layers, under cloud layers, at the tropopause, and at the surface. “Total”, “water”, and “ice” mean total clouds, water clouds only, and ice clouds only, respectively.

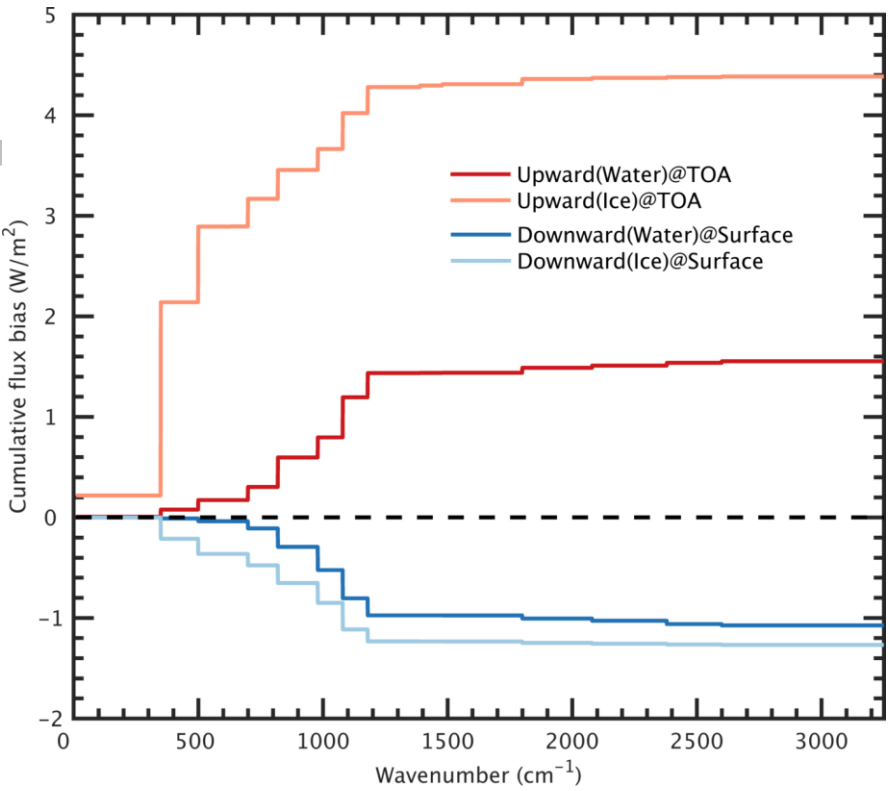

Figure 7. Cumulative biases of upward flux at the TOA (red or orange) and downward flux at the surface (blue or light blue) from 10 to 3250 cm^{-1} for water and ice clouds in 2010. Water (ice) means flux biases contributed by water (ice) clouds only.

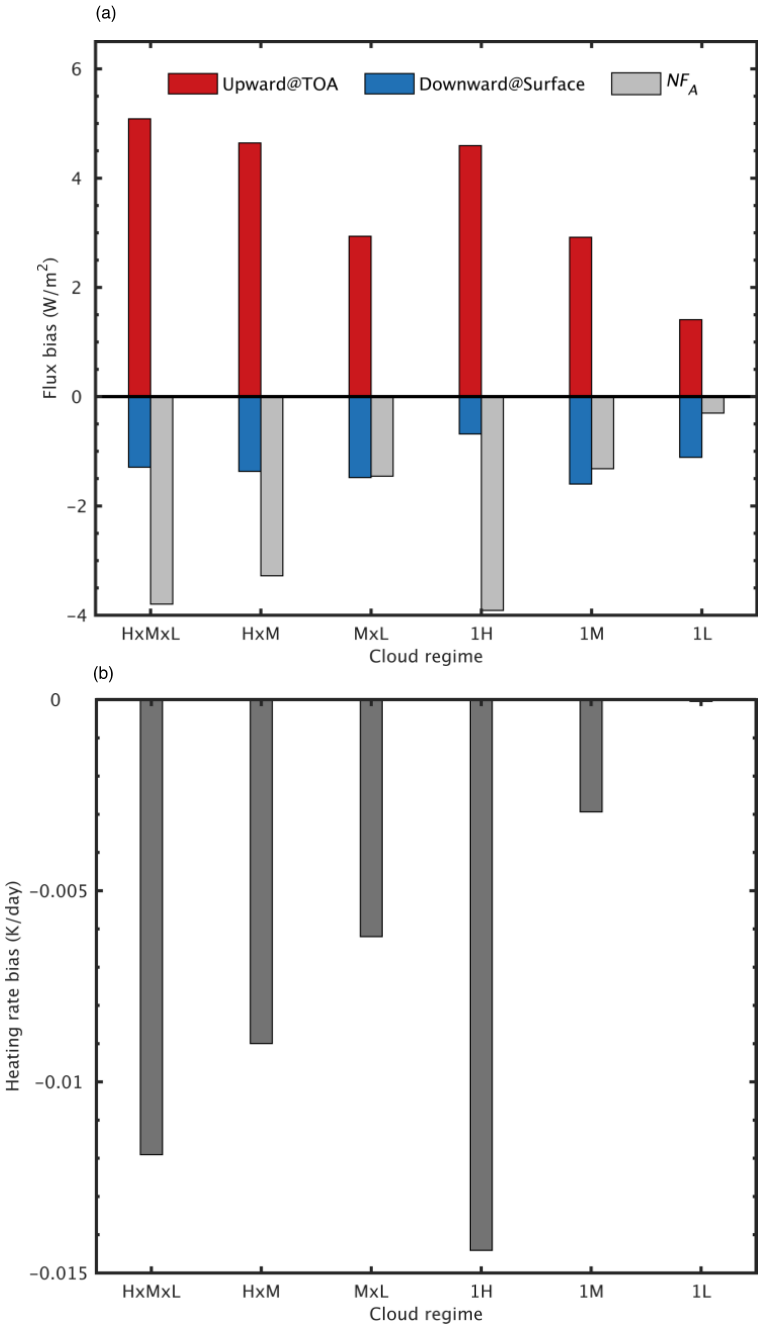

Figure 8. Annual global mean biases for 6 cloud regimes in 2010 of (a) upward flux at the TOA (red), downward flux at the surface (blue), and net flux into the atmosphere (grey), and (b) mean heating rate through the whole atmosphere column. 1H, 1M, and 1L indicate single-layer high, middle, and low cloud, respectively. HxMxL, HxM, and MxL mean cloud layers are continuous from high to low, high to middle, and middle to low regions, respectively.

Figure 1.

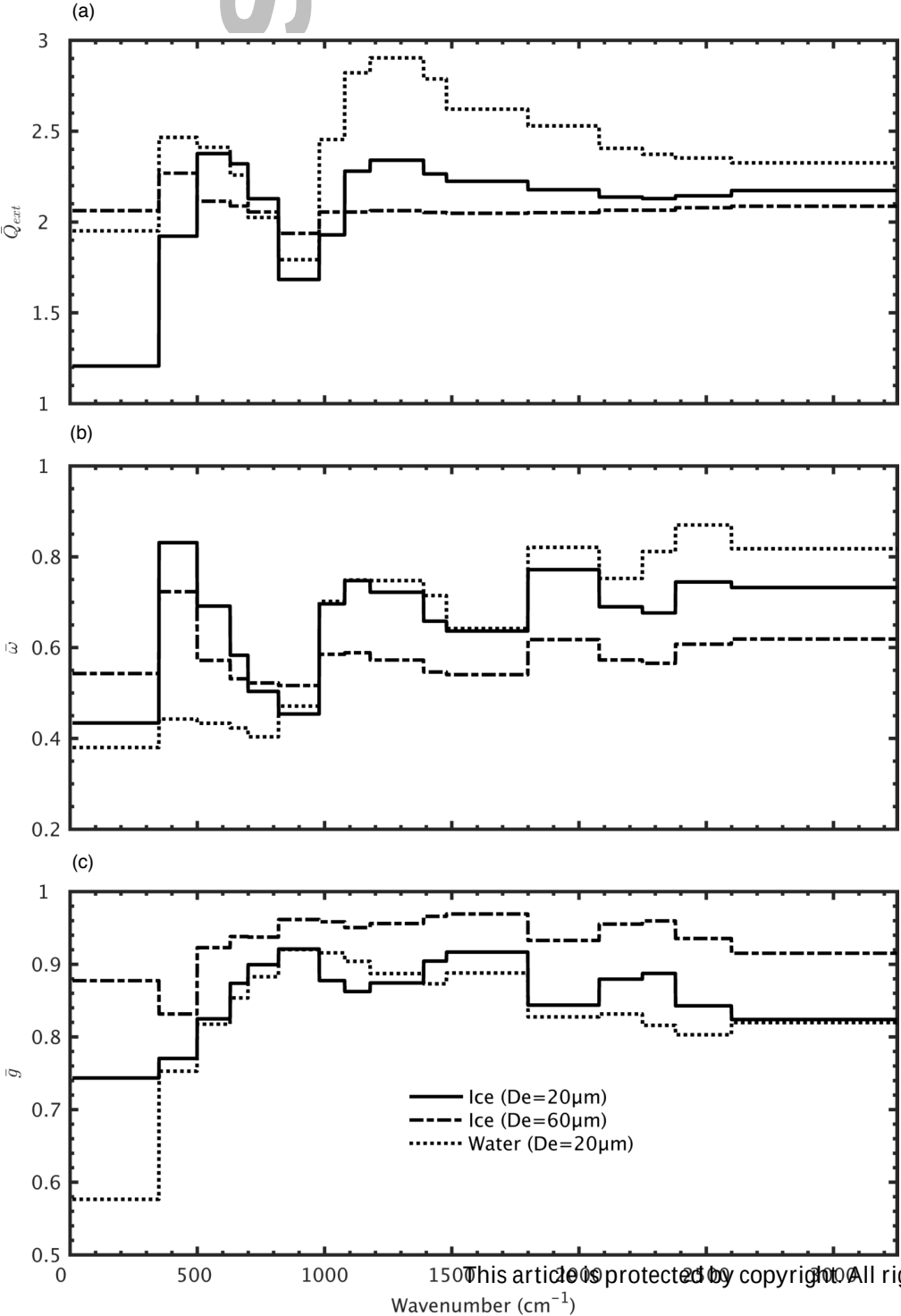

Figure 2.

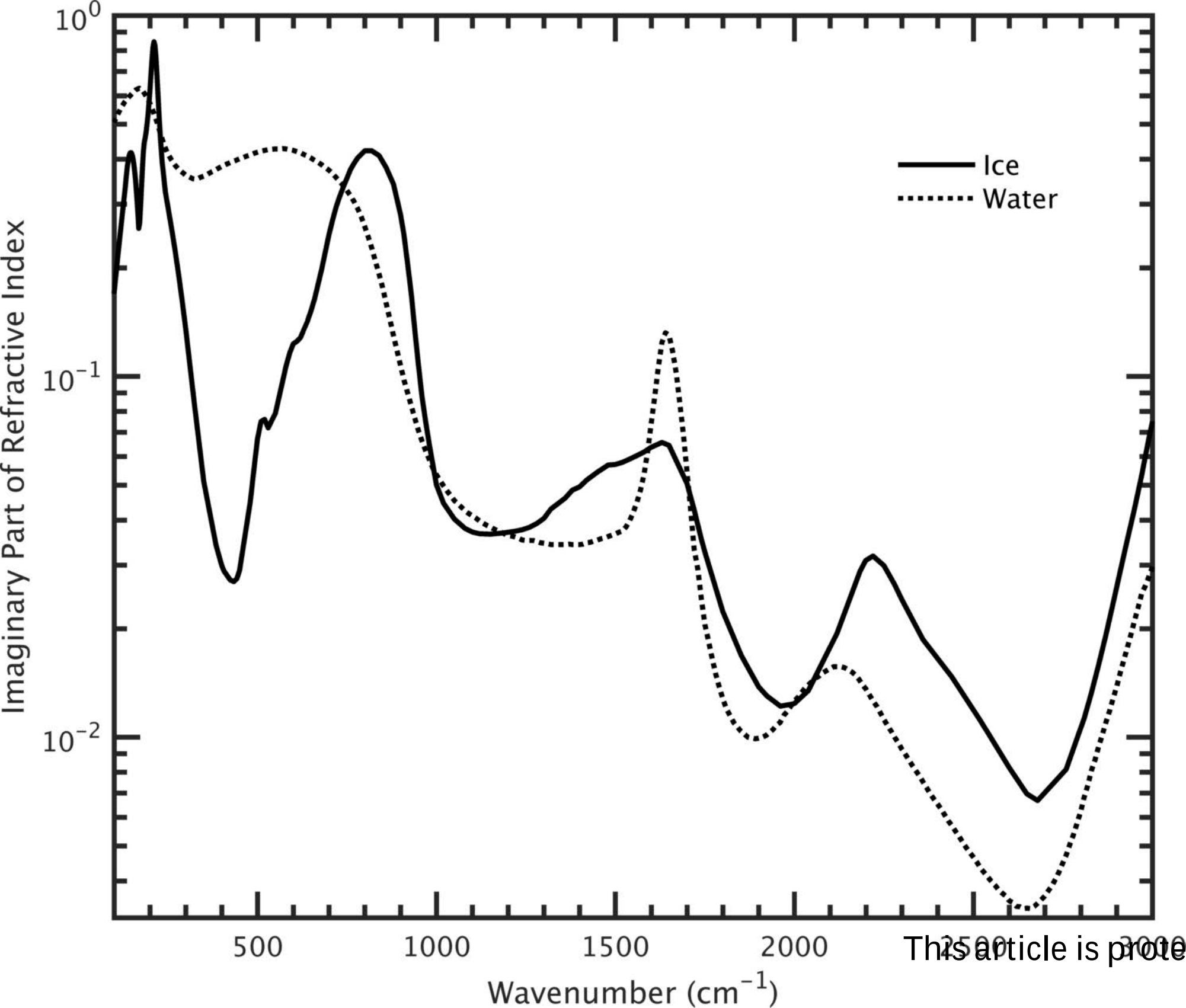

Figure 3.

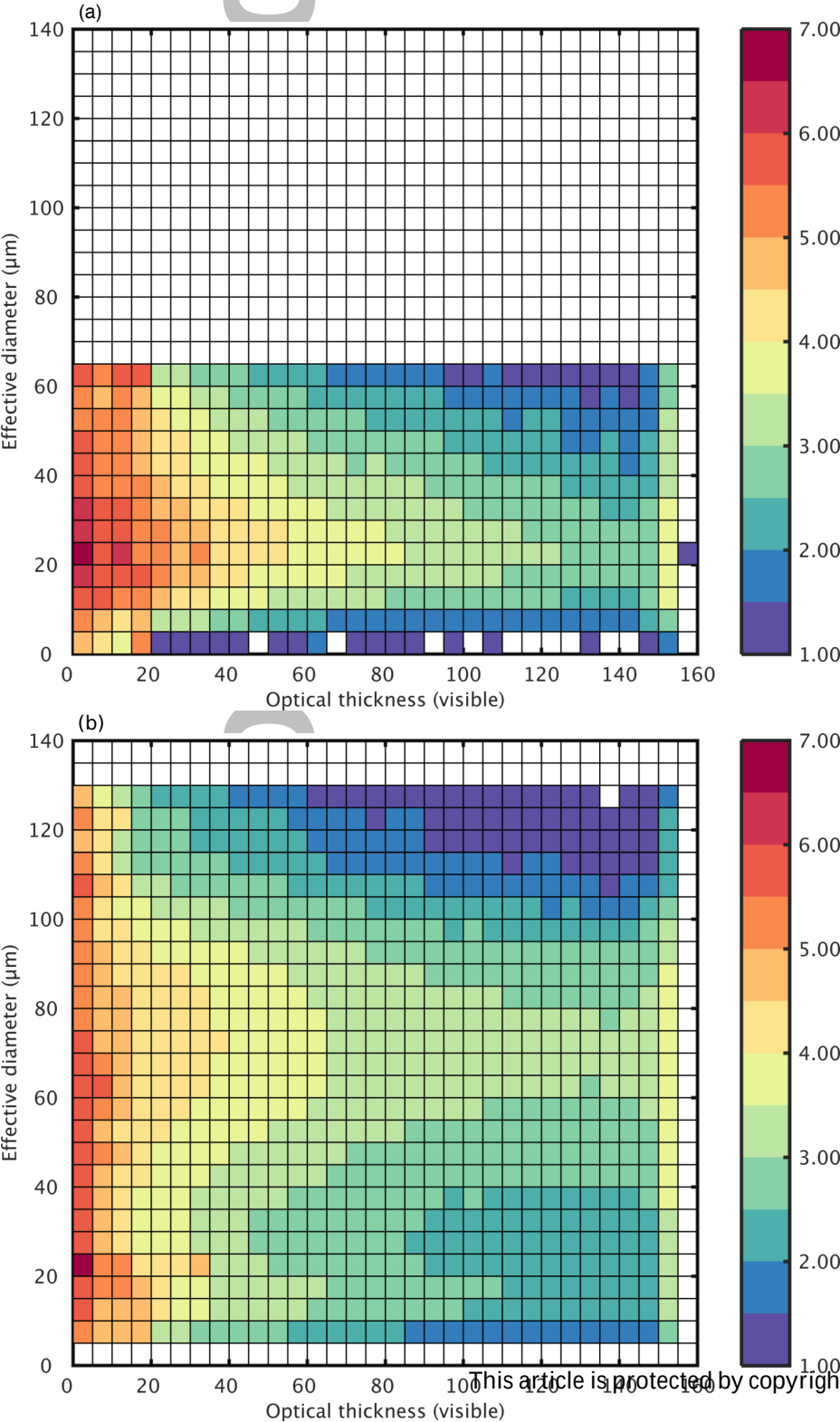

Figure 4.

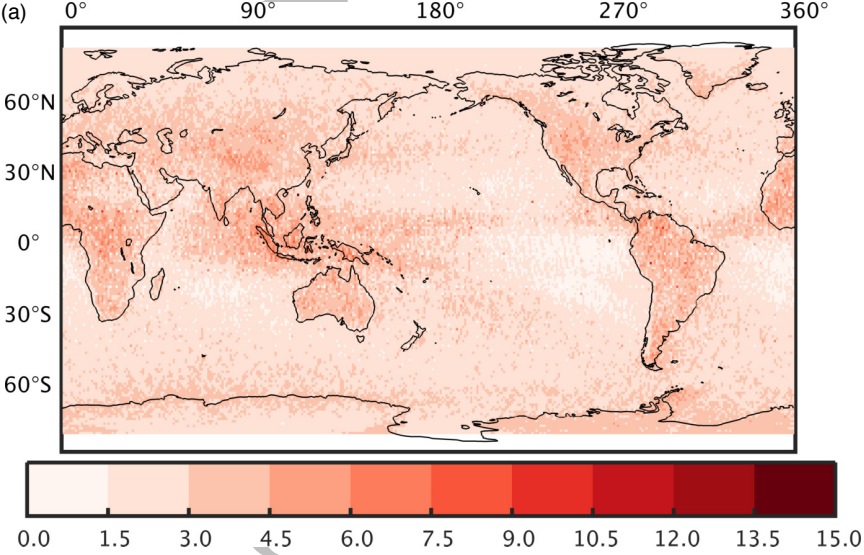

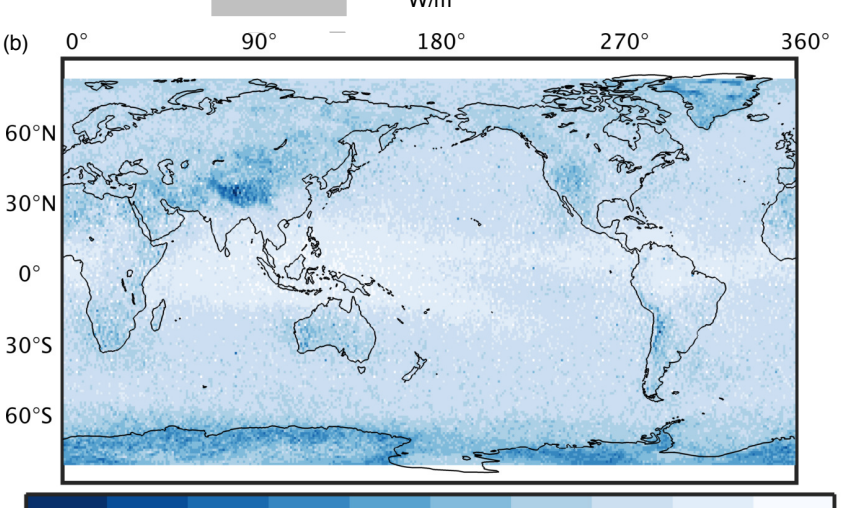

Figure 5.

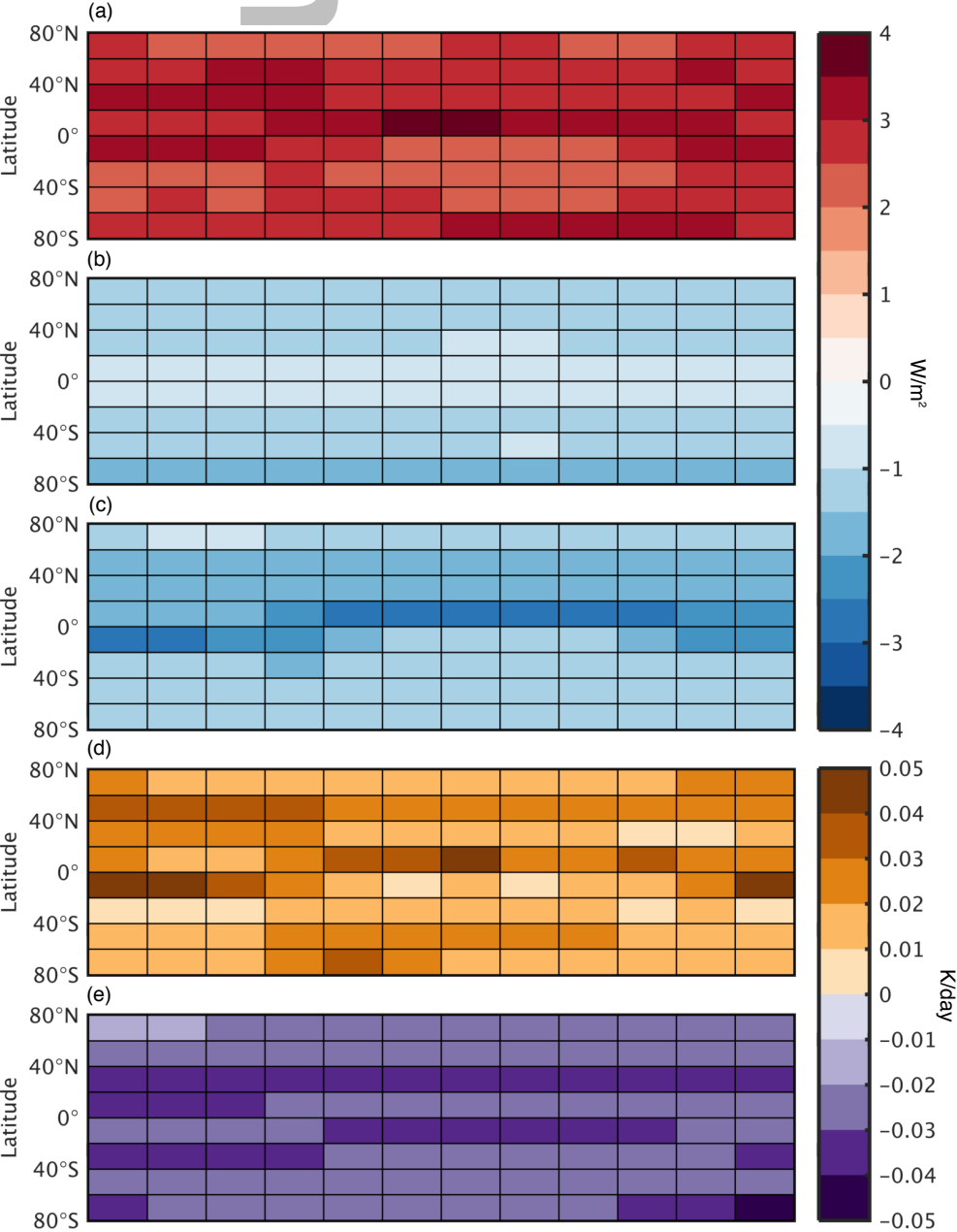

Figure 6.

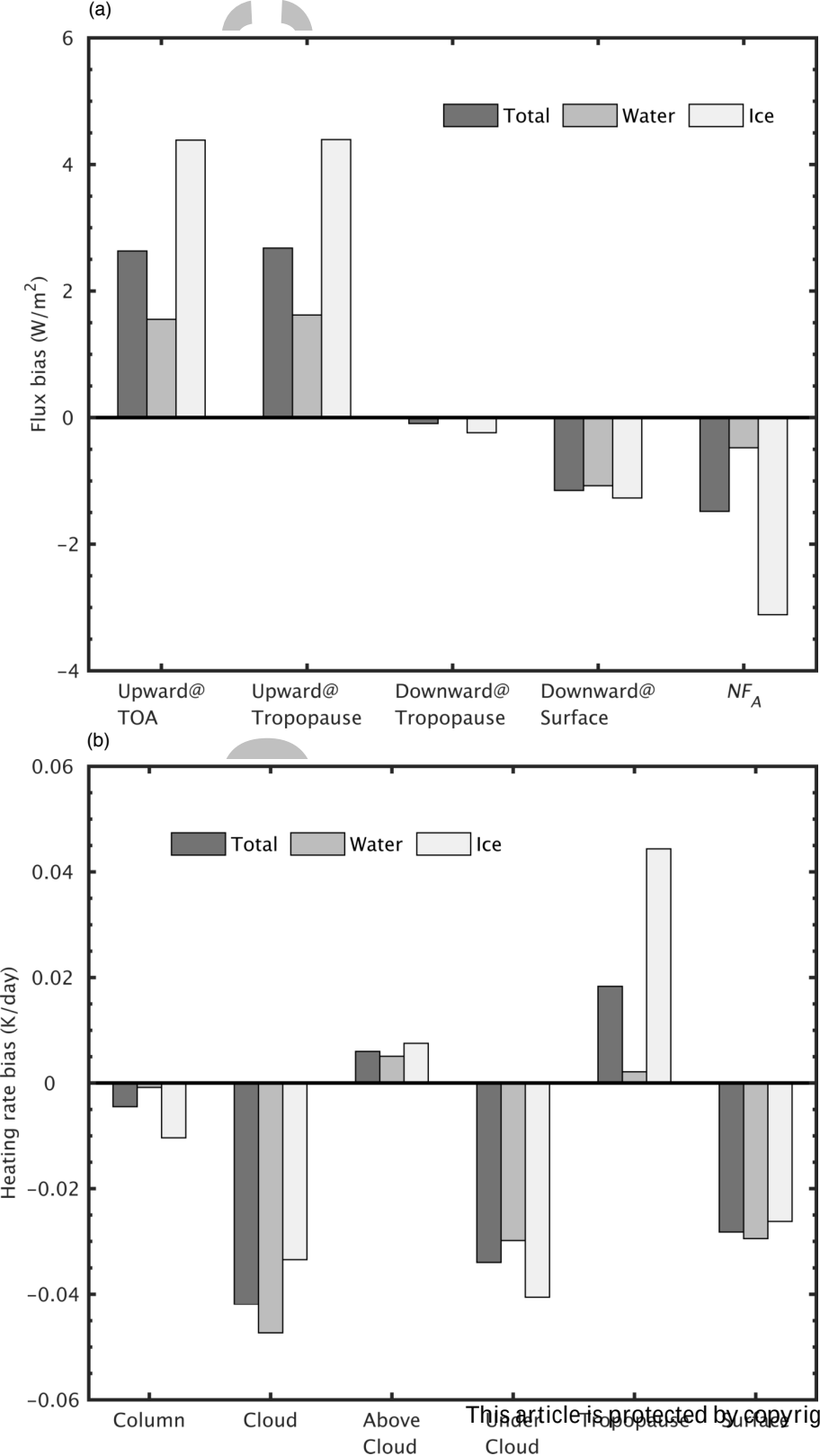

Figure 7.

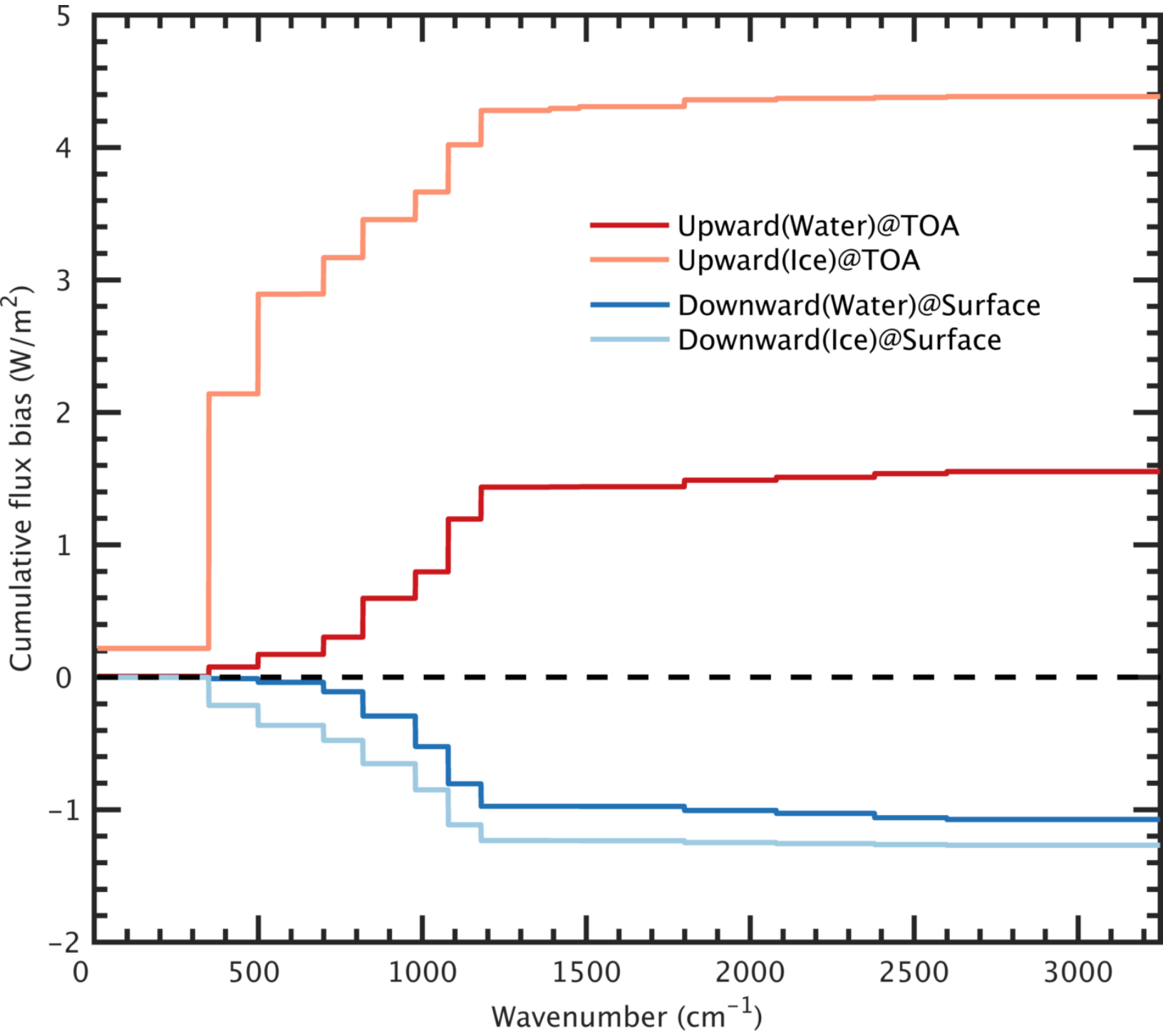

Figure 8.